On the best volume fraction distributions for functionally graded cylinders, spheres and disks – A pseudospectral approach

Hassan Mohamed Abdelalim Abdalla, Djaffar Boussaa, Roberta Sburlati, Daniele Casagrande

Composite Structures 311 (2023) 116784

Contents lists available at ScienceDirect

Composite Structures

journal homepage: www.elsevier.com/locate/compstruct

On the best volume fraction distributions for functionally graded cylinders, spheres and disks – A pseudospectral approach

Hassan Mohamed Abdelalim Abdalla [a,*], Djaffar Boussaa [b], Roberta Sburlati [c], Daniele Casagrande [a]

[a] Polytechnic Department of Engineering and Architecture, University of Udine, Via delle Scienze 206, 33100 Udine, Italy
[b] Aix Marseille Univ, CNRS, Centrale Marseille, LMA UMR 7031, Marseille, France
[c] Department of Civil, Chemical and Environmental Engineering, University of Genova, Via Montallegro 1, 16145 Genova, Italy

ARTICLE INFO

Keywords:
Functionally graded materials
Thermomechanical loads
Optimization
Optimal control
Pseudospectral approach
Plane elasticity

ABSTRACT

The paper is devoted to the optimization of axisymmetric structures made of functionally graded materials and subject to mechanical and thermal loads. The novelty of the results is that the volume fraction distribution is not limited to a power-law variation, as in most of the works available in the literature, but can be any (piecewise continuous) function. This approach leads to an intrinsic tailoring approach, in the sense it occurs without prefixing the spatial distribution of effective mechanical properties a priori, and therefore exploiting at best the inhomogeneity of functionally graded material. After recalling the governing equations and showing some recent results concerning candidate solutions for the optimal volume fraction distribution in some particular cases, several instances of the optimization problems aiming at minimizing occurring maximum stresses are formulated. We show that all these formulations can be treated within the same numerical approach based on the so-called pseudospectral methods. In the last part of the paper we describe how these methods have been effectively applied to the considered problems and we discuss the yielded solutions comparing them, where possible, with power-law solutions.

1. Introduction

The paper develops a numerical approach to optimize the volume fraction distribution for axisymmetric structures made of functionally graded materials (FGMs) under mechanical and thermal loads. These materials are classified as composite materials whose microstructure, and hence effective properties, are allowed to vary along a prescribed direction. Generally, this variation in material properties is exclusively examined according to specific functions of the volume fractions of the constituents with respect to spatial coordinates [1]. Volume fractions are in turn linked to the material properties through different models ranging from explicit traditional rules of mixture to models developed under micromechanical principles.

The above mentioned optimization problem has been given a considerable attention in the last years. In particular, the overwhelming studies consider the heterogeneity factors of prefixed variation models of the volume fractions as control variables so that a certain mechanical performance is enhanced. For instance, an optimized response for a disk with variable density through the radial direction has been reported in [2] by applying classical and heuristic optimization methods. A finite-element-based optimization of a pressure vessel consisting of a finite-length hollow cylinder with hemispherical ends has been performed in [3]. A combination of a co-evolutionary particle swarm optimization approach coupled with a differential quadrature method is applied in [4] to minimize stress and displacement fields in a disk under thermoelastic loads. The thermomechanical analysis and optimization of functionally graded rotating hollow disks is dealt with in [5] by using the sequential quadratic programming method.

In these latter works, heterogeneity factors are the exponents associated with the power-law property distributions. Due to their analytical tractability, the resulting elastic fields are amenable to numerical optimization by gradient-based methods or meta-heuristic algorithms, yet imposing considerable limitations to the generalization of the optimization procedure. These limitations shed the light on the importance of providing optimization methods consisting in the search for the best volume fractions as functions of the spatial direction, and not merely for the tuning values of factors associated with prefixed models. For instance, the simultaneous optimization of material properties and structural layout for an elastic continuum with maximum structural

* Corresponding author.
E-mail addresses: abdalla.hma@spes.uniud.it (H.M.A. Abdalla), boussaa@lma.cnrs-mrs.fr (D. Boussaa), roberta.sburlati@unige.it (R. Sburlati), daniele.casagrande@uniud.it (D. Casagrande).

https://doi.org/10.1016/j.compstruct.2023.116784
Received 8 November 2022; Received in revised form 6 January 2023; Accepted 9 February 2023
Available online 16 February 2023

stiffness is formulated and analyzed in [6]. The optimization of a two-phase isotropic composite material under time-dependent thermomechanical loadings, with no a priori assumptions regarding the spatial distribution of each phase, is addressed in [7]. In [8], an algorithm is proposed to minimize the time-averaged stress energy of a two-phase composite under dynamic loading. A three-layer cylinder consisting of a functionally graded interlayer sandwiched between a metallic layer and a ceramic layer is considered in [9], where the problem of finding the interlayer composition profile which minimizes the stresses resulting from material property mismatch and induced in the cylinder by temperature and pressure loading is addressed. In [10], thermoelastic bodies composed of two-constituent FGMs under steady-state conditions are considered and the problem of the optimal choice of composition profile is addressed. Moreover, in [11], the inverse problem of finding the variation with the radius of the shear modulus so that the difference between the radial and the hoop stress satisfies a particular relation along the radius is considered. In [12], the shear modulus such that stresses radially evolve in rubber-like cylinders and spheres within a more general functional constraint is sought. The mass optimization of FGM plates under deflection and stress requirements has been addressed in [13], where a piecewise cubic interpolation has been used to calculate volume fractions of constituent material phases. In [14], a novel phase-field topology optimization algorithm based on a graded material definition is introduced for the optimization of cantilevered beams. The size and shape optimization of FGM plates have been numerically performed in [15] by genetic algorithms and in [16,17] by means of isogeometric approaches. A similar work aiming at enhancing the buckling behavior of toroidal shells has been recently presented in [18]. Eventually, coated structures with layer-wise graded lattice infill have been analyzed in [19] by means of topology optimization for maximizing the fundamental eigenfrequency.

The present article addresses the problem of finding the best volume fractions of the constituents for axisymmetric FGM cylinders, disks and spheres. These models are frequently employed when it is desired to study the mechanical behavior of, e.g., pipes, gears, vessels or turbine rotors under thermomechanical loads, where the material is assumed to be locally isotropic, functionally graded in the radial direction and subject to mechanical and thermal loads. It is worth noting that the volume fraction distribution is an unknown function of the radial coordinate, offering a material tailoring approach for FGMs. In [20], the problem of minimizing the maximum occurring equivalent stress for cylinders loaded under the plane stress condition has been formulated in the context of dynamic optimization theory and has been solved by means of Pontryagin's Principle. The problem has been subsequently generalized in [21] to take into consideration other load conditions and the effect of different models linking volume fractions to effective mechanical properties. Moreover, the thermomechanical behavior of pressurized spherical vessels has been enhanced in terms of stress reduction in [22] by adopting functionally graded internal coatings rather than entirely graded spherical vessels. Here, motivated by the conclusions made in [23], the problem of minimizing peak stresses in the aforementioned studies (and disks) is formulated and solved numerically. Optimization problems are formulated by referring to two different formulations. The first one is exclusively based on the radial stress and its derivative along the radial direction. This formulation, under some mild hypotheses, led to candidate solutions in [20,21] analytically. In this article, some critical remarks on these solutions are reported, revealing that the approach might be enhanced if resorting to another formulation given in terms of both radial stress and radial displacement as state variables of the problem. It is desired to recall that both formulations, besides leading to solutions which perform better than classic volume fraction distributions, present promising results in terms of stress reduction, as shown below.

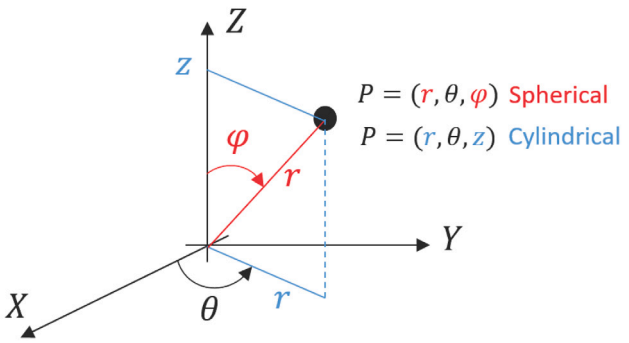

Fig. 1. A representation of the cylindrical and spherical coordinate systems.

2. Basic equations

2.1. Geometry

Consider a radially graded axisymmetric body whose microstructure compositionally grades from a ceramic to a metallic material, whose generic mechanical properties are denoted by P_c and P_m, respectively, and let R_i and R_o denote the inner and outer radii, respectively. Let the radial coordinate be denoted by r. For the cylinder and the disk, let the circumferential (or hoop) and axial coordinates be denoted by θ and z, respectively, while, for the sphere, let θ and φ be the polar and azimuthal angles, respectively (see Fig. 1). If the body is subject to an axisymmetric load, then deformations are also axisymmetric, namely they vary only in the radial direction. More specifically, both strains and stresses, denoted by ϵ_k and σ_k (with $k = r, \theta, z, \varphi$), respectively, are functions of r only. Moreover, for the pressured hollow spheres polar and azimuthal stresses are equal to each other.

2.2. Effective properties

As far as effective mechanical properties are concerned, several models that permit their evaluation from volume fractions are available in the literature, ranging from bounding methods to mean-field methods [24]. Although these models may give dissimilar estimates [25], they have the advantage of providing explicit formulas for the effective properties. The simplest models are derived from elasticity principles (minimum of potential energy and maximum complementary energy) assuming no interaction exists between metallic and ceramic phases, leading to linear combination (Voigt model) and a harmonic mean estimation (Reuss model) with respect to the volume fractions. The exclusive choice of Voigt and Reuss models in the present article is however motivated by the fact that they could offer a lower and an upper estimate for effective properties obtained by other models. The resulting models give rise to the following rules of mixture [1]

$$P(r) = P_\mathrm{m} V_\mathrm{m}(r) + P_\mathrm{c} V_\mathrm{c}(r) \tag{1}$$

and

$$P(r) = \frac{P_\mathrm{c} P_\mathrm{m}}{P_\mathrm{m} V_\mathrm{c}(r) + V_\mathrm{m}(r) P_\mathrm{c}}\,, \tag{2}$$

for Voigt and Reuss models, respectively, where $V_\mathrm{c}(r)$ and $V_\mathrm{m}(r)$ are the ceramic and metallic volume fractions at the generic radius r, related to each other by the relation [1]

$$V_\mathrm{c}(r) + V_\mathrm{m}(r) = 1\,. \tag{3}$$

Table 1
Hookean coefficients d_{ij} $(i,j=1,2)$ associated with Eq. (6) in terms of Young's modulus and Poisson's ratio.

	Cylinder ($\sigma_z=0$)	Cylinder ($\varepsilon_z=0$)	Sphere
d_{11}	$1/E$	$(1-\nu^2)/E$	$1/E$
d_{12}	$-\nu/E$	$-\nu(1+\nu)/E$	$-2\nu/E$
d_{21}	$-\nu/E$	$-\nu(1+\nu)/E$	$-\nu/E$
d_{22}	$1/E$	$(1-\nu^2)/E$	$(1-\nu)/E$

2.3. Governing elasticity equations

Most of the following analyses take place in the framework of linear elasticity by considering cylindrical bodies in plane state, with the hypothesis that strains or stresses are zero along the z-direction. Such behaviors are referred to as plane strain and plane stress, respectively [26]. We remind that the plane strain condition requires that ends of the cylinders are subjected to frictionless contact boundary conditions and the stress σ_z is determined by the constitutive equations. Of course, there are comparatively few practical applications in which a cylinder with plane ends is constrained between frictionless and fixed ends, but, using the Saint Venant's principle, the plane strain assumption can be used in an approximate sense for a cylinder with any end conditions, provided that the length of the cylinder is large compared with its cross-sectional dimensions [26]. On the other hand, examples satisfying the plane stress condition are approached in the limit as the thickness of the cylinder is small in comparison to the transversal section. This assumption allows to overcome the inconsistency of the out-of-plane behavior of the plane state formulation. Thin disks or rings belong to this category. Both plane state conditions can be formulated by following either the so-called Navier or Beltrami–Michell approaches, so far as boundary conditions are expressed in terms of radial displacements or stresses, respectively [27].

According to the linear elasticity theory, in absence of body forces and assuming axisymmetric loading condition, the equilibrium equation in the radial direction for cylindrical bodies may be written in the form [28]

$$\sigma_r'(r)+\frac{\chi[\sigma_r(r)-\sigma_\theta(r)]}{r}=0\,, \tag{4}$$

where the prime symbol denotes the first derivative with respect to r and $\chi=1$. This equation assumes similar form for spherical bodies with axisymmetric conditions by assuming $\chi=2$; bodies that we will also analyze in this paper. Moreover, the strain–displacement equations are [28]

$$\varepsilon_r(r)=u'(r)\,,\quad \varepsilon_\theta(r)=u(r)/r\,, \tag{5}$$

where u is the radial displacement. The stress–strain relation is written in the form [28]

$$\begin{pmatrix}\varepsilon_r\\ \varepsilon_\theta\end{pmatrix}=\begin{bmatrix}d_{11} & d_{12}\\ d_{21} & d_{22}\end{bmatrix}\begin{pmatrix}\sigma_r\\ \sigma_\theta\end{pmatrix}, \tag{6}$$

where the Hookean coefficients d_{11}, d_{12}, d_{21} and d_{22} are listed in Table 1 in terms of Young's modulus E and Poisson's ratio ν, for cylinders loaded in the plane stress ($\sigma_z=0$) and plane strain ($\varepsilon_z=0$) conditions and for spheres with axisymmetric loading conditions ($\sigma_\theta=\sigma_\varphi$) [28].

3. Optimization problems

In this Section, the statement and mathematical formulation of the optimization problems are addressed for pressurized cylinders and spheres and rotating disks. A schematic representation for each model is shown in Fig. 2 together with the applied loads and boundary conditions.

3.1. Internally pressurized cylinders

Let the axisymmetric body described in Section 2.1 be an internally pressurized cylinder. In order to formulate the optimization problem described in the Introduction in the context of dynamic optimization theory, a state–space representation, boundary conditions and a objective functional are needed. To this purpose, two different formulations are introduced concerning different choices of the state variables. In the first formulation the radial stress and its derivative are assumed as elastic states variables (stress formulation) while in the second formulation we assume as state variable radial displacement and radial stress (mixed formulation).

3.1.1. Stress formulation for the cylinder

Reference is made to the formulation reported in [21], namely based on the Beltrami–Michell approach, where Poisson's coefficient has been assumed constant, elastic state variables are given by stresses and their derivatives and the control function is the rate of change of the ceramic volume fraction with respect to r, namely $\frac{dV_c(r)}{dr}$, herein denoted by $\mathrm{v_c}(r)$. In particular, the radial strain in Eq. (5), together with the constitutive relations (6) and the equilibrium Eq. (4) yield

$$\mathcal{O}\sigma_r(r)=0 \tag{7}$$

where $\mathcal{O}$ is a differential operator given by [21]

$$\mathcal{O}(\bullet)=r^2(\bullet)''+r[3-r\Gamma(r)\mathrm{v_c}(r)](\bullet)'-\tilde{\nu}\Gamma(r)\mathrm{v_c}(r)r(\bullet) \tag{8}$$

and $\tilde{\nu}=1-\nu$ and Γ is a function whose explicit expression is derived from the involved rule of mixture; in particular,

$$\Gamma(r)=\frac{1}{\frac{E_m}{E_c-E_m}+V_c(r)}$$

and

$$\Gamma(r)=\frac{E_c-E_m}{E_mV_c(r)+(1-V_c(r))E_c}$$

for Voigt and Reuss models, respectively (for justification, see [21]). Moreover, it is worth noting that the differential operator $\mathcal{O}$ for the plane strain condition is identical to (8) provided that $\tilde{\nu}$ is replaced by $\check{\nu}=1-\nu/\tilde{\nu}$ (see [21]).

Introducing the elastic state variables $y_1=\sigma_r$, $y_2=d\sigma_r/dr$ and $y_3=V_c$, the differential Eq. (7), which serves as differential constraints and should be satisfied while searching for the optimal solution, may be recast as

$$\begin{cases} y_1'(r)=y_2(r)\,,\\ y_2'(r)=\Gamma(r)\left(y_2(r)+\tilde{\nu}\dfrac{y_1(r)}{r}\right)\mathrm{v_c}(r)-\dfrac{3y_2(r)}{r}\,,\\ y_3'(r)=\mathrm{v_c}(r)\,. \end{cases} \tag{9}$$

As far as boundary conditions are concerned, $y_1(R_i)$ and $y_1(R_o)$ can be deduced from the radial stresses at R_i and R_o, namely

$$y_1(R_i)=-p_i\,,\quad y_1(R_o)=0\,, \tag{10}$$

where p_i is the internal pressure, while $y_2(R_i)$ and $y_2(R_o)$ are unknown. Regarding y_3, if the cylinder is compositionally graded from ceramic to metal, then

$$y_3(R_i)=1\,,\quad y_3(R_o)=0\,. \tag{11}$$

Taking into account the plane stress condition and using the above introduced state variables, the equivalent Tresca stress may be written as

$$\sigma_{eq}^T(r)=|\sigma_\theta(r)-\sigma_r(r)|=|y_1(r)+ry_2(r)-y_1(r)|=|ry_2(r)|.$$

Since the body is pressurized only internally, y_1 strictly increases along the radius, and therefore $y_2>0$. Consequently, the absolute value can be omitted and the minimization of $y_2(R_i)$ leads to the minimization of

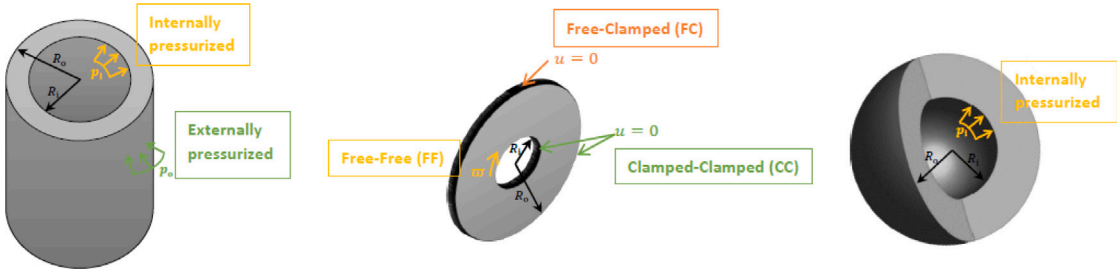

Fig. 2. A schematic representation for the considered axisymmetric bodies (cylinders, disks and spheres).

the internal Tresca stress. The same problem can be stated within the plane strain condition, taking into account that

$$\sigma_z(r) = \nu(\sigma_r(r) + \sigma_\theta(r)) = \nu(2y_1(r) + r y_2(r)).$$

According to [29], there are few optimization studies in which the manufacturability cost is taken into consideration. Adding technological constraints to optimization studies is highly recommended as it leads to more practical designs with large-scale production prospects. To this purpose, FGM regions with a steep composition gradient are more difficult and therefore more expensive to manufacture. The slope, and thus the cost, can be controlled by imposing bounds on the values that the composition gradient can take. As a consequence, it is reasonable to assume that $\mathrm{v_c}$ be constrained in an admissible range of values. More precisely, we assume, for all values of r, $\mathrm{v_c} \in [\mathrm{v_-}, \mathrm{v_+}]$, whose bounds $\mathrm{v_-}$ and $\mathrm{v_+}$ can be deduced from fixed radial property variations or from technological process data. Hence, the optimization problem can now be stated formally as follows.

Problem 1. Find the distribution of the derivative of the ceramic volume fraction $\mathrm{v_c^*}(r)$ that minimizes the Tresca stress at the inner surface, i.e.,

$$\begin{aligned}
&\min_{\mathrm{v_c}(r)} \quad y_2(R_\mathrm{i}) \\
&\text{s.t.} \quad y_1'(r) = y_2(r)\,, \\
&\qquad y_2'(r) = \Gamma(r)\left(y_2(r) + \tilde{\nu}\frac{y_1(r)}{r}\right)\mathrm{v_c}(r) - \frac{3y_2(r)}{r}\,, \\
&\qquad y_3'(r) = \mathrm{v_c}(r)\,, \\
&\qquad y_1(R_\mathrm{i}) = -p_\mathrm{i}\,, \\
&\qquad y_1(R_\mathrm{o}) = 0\,, \\
&\qquad y_3(R_\mathrm{i}) = 1\,, \\
&\qquad y_3(R_\mathrm{o}) = 0\,, \\
&\qquad \mathrm{v_-} \le \mathrm{v_c}(r) \le \mathrm{v_+}\,, \\
&\qquad 0 \le y_3(r) \le 1\,,
\end{aligned} \tag{12}$$

where R_i, R_o, $\mathrm{v_-}$, $\mathrm{v_+}$, p_i and $\tilde{\nu}$ are given constants and $\Gamma(r)$ is a specified function depending on the rule of mixture.

3.1.2. A proposed analytical solution

Pontryagin's principle has been applied to Problem 1 in [21]. The optimal change rate of the function $\mathrm{v_c^*}$, i.e., the one which minimizes the objective functional $y_2(R_\mathrm{i})$ is, among all admissible functions, the one which, at any value of r, minimizes the corresponding Hamiltonian function $\mathcal{H}(r, \mathbf{y}, \mathbf{p}, \mathbf{m}, \mathrm{v_c})$, given by [21]

$$\begin{aligned}
\mathcal{H}(r, \mathbf{y}(r), \mathbf{p}(r), \mathbf{m}(r), \mathrm{v_c}(r)) &= \mathcal{S}(r, \mathbf{y}(r), \mathbf{p}(r), \mathbf{m}(r)) \\
&\quad + \mathcal{Q}(r, \mathbf{y}(r), \mathbf{p}(r), \mathbf{m}(r))\,\mathrm{v_c}(r)\,,
\end{aligned} \tag{13}$$

where $\mathbf{p}$ is the vector of costate variables associated with the elastic states variables $\mathbf{y}$ and $\mathbf{m}$ is the vector of Lagrange multipliers associated with the inequality constraints, all functions of r, whereas $\mathcal{S}$ and $\mathcal{Q}$ are functions of these vectors, whose explicit expressions depends on the problem under consideration. Nevertheless, it is worth noting that the problem is characterized by a linear Hamiltonian function with respect to $\mathrm{v_c}$ and since the set of admissible values for $\mathrm{v_c}$ is compact, Pontryagin's Principle yields extremal solution for the minimization of (13). More precisely, the optimal rate of change $\mathrm{v_c^*}$ is defined by

$$\mathrm{v_c^*}(r) = \arg\min_{\mathrm{v_c}} \mathcal{H}(r) = \begin{cases} \mathrm{v_-}\,, & \text{if } \mathcal{Q}(r) > 0\,, \\ \mathrm{v_+}\,, & \text{if } \mathcal{Q}(r) < 0\,. \end{cases} \tag{14}$$

If $\mathcal{Q}(\bar{r}) = 0$ for some $\bar{r}$ then the value of $\mathrm{v_c^*}(\bar{r})$ cannot be determined by the Pontryagin's principle. However, two scenarios are possible, according to the local behavior of $\mathcal{Q}$ in the neighborhood of $\bar{r}$. In the first one, $\mathcal{Q}$ crosses the value zero in $\bar{r}$ passing from a positive value (for $r < \bar{r}$) to a negative one (for $r > \bar{r}$) (or viceversa). In this case the value of $\mathrm{v_c^*}(\bar{r})$ switches instantaneously from one extreme value to the other one yielding to what is usually referred to as "bang–bang" solution. The point $\bar{r}$ is called "switching point". The value of $\mathrm{v_c^*}(\bar{r})$ is not crucial to determine, through (9), the optimal trajectories of the state variables: any two different values lead to the same trajectories. In the second scenario, $\mathcal{Q} = 0$ in a whole interval (containing $\bar{r}$). In this case, the solution, called "singular", shall be found from other considerations.

For the sake of analytical tractability, the investigation of the second scenario is omitted. Hence, recalling the definition of $\mathrm{v_c}$, the optimal ceramic volume fraction V_c^* turns out, under the adopted assumptions, to be piecewise linear with respect to r. This conclusion is particularly interesting since piecewise linear profiles are among the simplest to manufacture. However, Eq. (14) does not yet provide the explicit expression of the optimal solution; in fact, it is clear that in order to know the explicit value of $\mathrm{v_c^*}$ for any value of r one should know the value of $\mathcal{Q}$. Hence, a special attention has been drawn in [21] to the case in which $\mathcal{Q}$ has only one root, namely when the optimal solution admits a single switching point. Denoting by $\bar{v}$ the rate of the linear variation between $y_3(R_\mathrm{i}) = 1$ and $y_3(R_\mathrm{o}) = 0$, namely

$$\bar{\mathrm{v}} = -\frac{1}{R_\mathrm{o} - R_\mathrm{i}}\,,$$

if $\bar{\mathrm{v}} \in [\mathrm{v_-}, \mathrm{v_+}]$, two optimal solutions are possible. The first one is characterized by a subinterval in which $\mathrm{v_c} = \mathrm{v_+}$ followed by a subinterval in which $\mathrm{v_c} = \mathrm{v_-}$, while the other one presents the opposite situation (a first subinterval where $\mathrm{v_c} = \mathrm{v_-}$ followed by a subinterval where $\mathrm{v_c} = \mathrm{v_+}$). Moreover, the corresponding switching points $\tilde{r}$ and $\hat{r}$ can be analytically determined as [21]

$$\tilde{r} = \frac{-1 - \mathrm{v_-} R_\mathrm{o} + \mathrm{v_+} R_\mathrm{i}}{\mathrm{v_+} - \mathrm{v_-}}\,, \quad \hat{r} = \frac{1 - \mathrm{v_-} R_\mathrm{i} + \mathrm{v_+} R_\mathrm{o}}{\mathrm{v_+} - \mathrm{v_-}}\,, \tag{15}$$

respectively.

A numerical example has been carried out concerning the design of a family of internally pressurized thick-walled FGM cylinders in [21], where the material variation has to be chosen to minimize the inner equivalent Tresca stress. Classic volume fraction variations, e.g., linear, sinusoidal and sigmoid, have been considered and then compared with the ones associated with the optimal solutions resulting from Pontryagin's Principle. A dedicated finite element model has been developed to numerically forecast the stress behavior under plane stress and plane strain conditions and for selected $R_\mathrm{o}/R_\mathrm{i}$ ratios. For different values of

v_-/v_+, it has been shown that one of the two aforementioned bang–bang solutions corresponds to the minimum value of $\sigma_{eq}^{T}(R_i)/p_i$, thus outperforming the variations commonly employed in the literature, while the other one can be discarded.

3.1.3. Critical remarks

Although optimal solutions perform better than classic property variations employed in the literature, the aforementioned formulation of the problem could suffer from some critical aspects. The first one concerns the absence of a criterion for the selection of v_- and v_+, whose values should comply with the constraint on the number of switching points, which in turn is unknown. In fact, it has been implicitly assumed that the function $\mathcal{Q}$ in (13) is either strictly increasing or strictly decreasing along r and this assumption aimed to favor the analytical tractability of the problem. Secondly, it is emphasized that the stress formulation is not of much help to determine whether the function $\mathcal{Q}$ identically vanishes in one or more finite intervals throughout the radial direction. Eventually, it is observed that the expression for optimal solutions (14) thus derived is paradoxically insensitive neither to whether the pressurized cylinder is exhibiting a plane stress or a plane strain load condition nor to the employed rule of mixture. In fact, the state–space representation, the boundary states, the Hamiltonian function and the optimal rate of change of the ceramic volume fraction for the plane strain condition are the same as those for the plane stress, provided that $\tilde{v}$ is replaced by $\check{v}$.

These considerations hint one to reconsider the optimization problem by means of a different formulation, possibly bypassing the exploitation of Pontryagin's Principle so that it overcomes the aforementioned shortcomings. To this purpose, a mixed formulation based on both Navier and Beltrami–Michell approaches is illustrated next.

3.1.4. Mixed formulation for the cylinder

Unlike the stress based formulation, elastic state variables are taken to be the radial displacement and the radial stress. Hereinafter, the variation of Poisson's ratio along the radial coordinate is included.

Firstly, the assumption of plane stress load condition is made. On the one hand, from Eqs. (5), (6) and (4), the radial strain can be expressed as

$$u'(r) = \frac{\sigma_r(r) - \nu(r)\sigma_\theta(r)}{E(r)} = \frac{\sigma_r(r) - \nu(r)[\sigma_r(r) + r\sigma_r'(r)]}{E(r)}. \tag{16}$$

On the other hand, the hoop strain and stress can be expressed as

$$\frac{u(r)}{r} = \frac{\sigma_\theta(r) - \nu(r)\sigma_r(r)}{E(r)}$$

and

$$\sigma_\theta(r) = \frac{E(r)}{1-\nu(r)^2}\left(\frac{u(r)}{r} + \nu(r)u'(r)\right),$$

respectively. Consequently, the hoop stress can be expressed in terms of the states as follows

$$\sigma_\theta(r) = E(r)\frac{u(r)}{r} + \nu(r)\sigma_r(r).$$

Consequently, the variation of the radial displacement and the radial stress with respect to the radial coordinate, in terms of the two states, are given by

$$u'(r) = -\frac{\nu(r)}{r}u(r) + \frac{1-\nu(r)^2}{E(r)}\sigma_r(r) \tag{17}$$

and

$$\sigma_r'(r) = \frac{E(r)}{r^2}u(r) + \frac{\nu(r)-1}{r}\sigma_r(r), \tag{18}$$

respectively.

Now, the assumption of a plane strain load condition is assumed. Here, the axial stress should be taken into account, whereas the axial strain is identically zero. This latter yields a relation between the three stresses, namely

$$\sigma_z(r) = \nu(r)(\sigma_r(r) + \sigma_\theta(r)). \tag{19}$$

From constitutive Eqs. (6) and (4), the variation of the radial displacement and radial stress with respect to the radial coordinate, in terms of the two states, are given by

$$u'(r) = \frac{\nu(r)}{(\nu(r)-1)r}u(r) + \frac{(1+\nu(r))(1-2\nu(r))}{(1-\nu(r))E(r)}\sigma_r(r) \tag{20}$$

and

$$\sigma_r'(r) = \frac{E(r)}{(1-\nu(r)^2)r^2}u(r) + \frac{2\nu(r)-1}{(1-\nu(r))r}\sigma_r(r), \tag{21}$$

respectively.

Unlike Problem 1, the maximum value for the Tresca equivalent stress is taken as the objective functional to be minimized and not that occurring at the inner radius. For the plane stress condition, the equivalent Tresca stress is given by

$$\sigma_{eq}^{T}(r) = \max\{|\sigma_\theta(r) - \sigma_r(r)|, |\sigma_\theta(r) - \sigma_z(r)|, |\sigma_r(r) - \sigma_z(r)|\}, \tag{22}$$

which, in the case of plane stress condition, is just reduced to the first argument at the right hand-side and can be written in terms of the two states as follows

$$\sigma_{eq}^{T}(r) = |\sigma_\theta(r) - \sigma_r(r)| = \left|E(r)\frac{u(r)}{r} + [\nu(r)-1]\sigma_r(r)\right| \tag{23}$$

and its maximum value can be approximated by the $\mathcal{P}$-norm, given by

$$\sigma_{eq,max}^{T} \approx \left\{\int_{R_i}^{R_o}\left(E(r)\frac{u(r)}{r} + (\nu(r)-1)\sigma_r(r)\right)^{\mathcal{P}} dr\right\}^{1/\mathcal{P}}. \tag{24}$$

Here and throughout $\mathcal{P}$ denotes an even positive integer greater than or equal to 2. As far as the plane strain condition is concerned, it is not trivial to decide which argument in Eq. (22) is dominant. Consequently, a potential candidate for the objective functional can be the maximum value for the hoop stress, which can be approximated as

$$\sigma_{\theta,max} \approx \left\{\int_{R_i}^{R_o}\left(\frac{1}{1-\nu(r)^2}\left(E(r)\frac{u(r)}{r} + \nu(r)(1+\nu(r))\sigma_r(r)\right)\right)^{\mathcal{P}} dr\right\}^{1/\mathcal{P}}. \tag{25}$$

Consequently, two optimization problems are formulated depending on the load condition. Introducing the state variables $y_1 = u$ and $y_2 = \sigma_r$, the problems for the plane stress and plane strain conditions assume respectively the following form.

Problem 2 (*Plane Stress Condition*)**.** Find the distribution of the metallic volume fraction $V_m^*(r)$ along the radial direction of the cylinder so that the maximum Tresca stress is minimized, i.e.,

$$\begin{aligned}
\min_{V_m(r)} \quad & \sigma_{eq,max}^{T} = \left\{\int_{R_i}^{R_o}\left(E(r)\frac{y_1(r)}{r} + (\nu(r)-1)y_2(r)\right)^{\mathcal{P}} dr\right\}^{1/\mathcal{P}} \\
\text{s.t.} \quad & y_1'(r) = -\frac{\nu(r)}{r}y_1(r) + \frac{1-\nu(r)^2}{E(r)}y_2(r), \\
& y_2'(r) = \frac{E(r)}{r^2}y_1(r) + \frac{\nu(r)-1}{r}y_2(r), \\
& y_2(R_i) = -p_i, \\
& y_2(R_o) = 0, \\
& 0 \le V_m(r) \le 1,
\end{aligned} \tag{26}$$

where R_i, R_o, p_i and $\mathcal{P}$ are given constants and $E(r)$ and $\nu(r)$ are linked to $V_m(r)$ through (1) or (2).

Problem 3 (*Plane Strain Condition*)**.** Find the distribution of the metallic volume fraction $V_m^*(r)$ along the radial direction of the cylinder so that

the maximum hoop stress attains its minimum value, i.e.,

$$\begin{aligned}
\min_{V_{\mathrm{m}}(r)} \quad & \sigma_{\theta,\max} = \left\{ \int_{R_{\mathrm{i}}}^{R_{\mathrm{o}}} \left(\frac{1}{1-\nu(r)^2} \left(E(r)\frac{y_1(r)}{r} \right.\right.\right. \\
& \left.\left.\left. + \nu(r)(1+\nu(r))y_2(r) \right) \right)^{\mathcal{P}} dr \right\}^{1/\mathcal{P}} \\
\text{s.t.} \quad & y_1'(r) = \frac{\nu(r)}{(\nu(r)-1)r} y_1(r) + \frac{(1+\nu(r))(1-2\nu(r))}{(1-\nu(r))E(r)} y_2(r), \\
& y_2'(r) = \frac{E(r)}{(1-\nu(r)^2)r^2} y_1(r) + \frac{2\nu(r)-1}{(1-\nu(r))r} y_2(r), \\
& y_2(R_{\mathrm{i}}) = -p_{\mathrm{i}}, \\
& y_2(R_{\mathrm{o}}) = 0, \\
& 0 \le V_{\mathrm{m}}(r) \le 1,
\end{aligned} \tag{27}$$

where R_{i}, R_{o}, p_{i} and $\mathcal{P}$ are given constants and $E(r)$ and $\nu(r)$ are linked to $V_{\mathrm{m}}(r)$ through (1) or (2).

3.2. Pressurized hollow spheres

Spherical FGM vessels have been given a considerable attention in the last years, under several acting loads [22,30,31]. Next, a dynamic optimization problem for the material tailoring of an internally pressurized sphere is presented. Note that the equilibrium equation is given by Eq. (4) with $\chi = 2$. Following the mixed formulation, a similar approach of Section 3.1 taking into account the equations for the spherical axisymmetry case. After some algebra, the formulation of the optimization problem assume the following form.

Problem 4. Find the distribution of the metallic volume fraction $V_{\mathrm{m}}^*(r)$ along the radial direction of the cylinder so that the maximum Tresca stress attains its minimum value, i.e.,

$$\begin{aligned}
\min_{V_{\mathrm{m}}(r)} \quad & \sigma_{\mathrm{eq,max}}^{\mathrm{T}} = \left\{ \int_{R_{\mathrm{i}}}^{R_{\mathrm{o}}} \left(E(r)\frac{y_1(r)}{r} + (\nu(r)-1)y_2(r) \right)^{\mathcal{P}} dr \right\}^{1/\mathcal{P}} \\
\text{s.t.} \quad & y_1'(r) = \frac{2\nu(r)}{(\nu(r)-1)r} y_1(r) + \frac{2\nu(r)^2+\nu(r)-1}{(\nu(r)-1)E(r)} y_2(r), \\
& y_2'(r) = \frac{2E(r)}{(1-\nu(r))r^2} y_1(r) + \frac{2(1-2\nu(r))}{(\nu(r)-1)r} y_2(r), \\
& y_2(R_{\mathrm{i}}) = -p_{\mathrm{i}}, \\
& y_2(R_{\mathrm{o}}) = 0, \\
& 0 \le V_{\mathrm{m}}(r) \le 1,
\end{aligned} \tag{28}$$

where R_{i}, R_{o}, p_{i} and $\mathcal{P}$ are given constants and $E(r)$ and $\nu(r)$ are linked to $V_{\mathrm{m}}(r)$ through (1) or (2).

3.3. Rotating hollow disks

The optimization of functionally graded hollow disks belongs to contemporary research challenges, as a significant amount of work has been done in order to understand their stress and strain behaviors [32–35]. By addressing the analysis to thin rotating disks only, the formulation of the optimization problem does not differ from that of Problem 2, provided that the centrifugal term $\rho(r)\varpi^2 r^2$ is added [28], where ϖ is the angular velocity and ρ denotes the density distribution along the disk, estimated by either (1) or (2). If the hollow disk is freely rotating, hence $y_2(R_{\mathrm{i}}) = y_2(R_{\mathrm{o}}) = 0$ and the formulation of the problem can be written as follows.

Problem 5. Find the distribution of the metallic volume fraction $V_{\mathrm{m}}^*(r)$ along the radial direction of the disk so that the maximum Tresca stress is minimized, i.e.,

$$\begin{aligned}
\min_{V_{\mathrm{m}}(r)} \quad & \sigma_{\mathrm{eq,max}}^{\mathrm{T}} = \left\{ \int_{R_{\mathrm{i}}}^{R_{\mathrm{o}}} \left(E(r)\frac{y_1(r)}{r} + (\nu(r)-1)y_2(r) \right)^{\mathcal{P}} dr \right\}^{1/\mathcal{P}} \\
\text{s.t.} \quad & y_1'(r) = -\frac{\nu(r)}{r} y_1(r) + \frac{1-\nu(r)^2}{E(r)} y_2(r), \\
& y_2'(r) = \frac{E(r)}{r^2} y_1(r) + \frac{\nu(r)-1}{r} y_2(r) - \rho(r)\varpi^2 r, \\
& y_2(R_{\mathrm{i}}) = 0, \\
& y_2(R_{\mathrm{o}}) = 0, \\
& 0 \le V_{\mathrm{m}}(r) \le 1,
\end{aligned} \tag{29}$$

where R_{i}, R_{o}, ϖ and $\mathcal{P}$ are given constants, $E(r)$, $\nu(r)$ and $\rho(r)$ are linked to $V_{\mathrm{m}}(r)$ through (1) or (2).

The disk considered in Problem 5 is a purely rotating disk, namely with no imposed displacement conditions on the inner and outer boundaries. For this reason, such disk is hereinafter referred to as free–free (FF) disk (see Fig. 2). In parallel, a similar problem associated with different boundary conditions on the radial displacement at inner and outer radii can be formulated by simply acting on the value of $y_1(R_{\mathrm{i}})$ and $y_1(R_{\mathrm{o}})$. In particular, we denote by free–clamped (FC) disks those rotating disks whose only the outer boundary is not allowed to radially deform. Similarly, rotating disks whose radial displacement at inner and outer boundaries are constrained are referred to as clamped–clamped (CC) disks (see Fig. 2).

4. Numerical procedure: A pseudospectral approach

Unlike Problem 1, Problems 2–5 are endowed with a nonlinear Hamiltonian function with respect to the metallic volume fraction. Necessary conditions for optimal solutions yield Hamiltonian boundary-value-problems [36], whose variables are nonlinearly coupled, thus jeopardizing the derivation of analytical solutions. Hence, numerical procedures are necessary to figure out optimal solutions.

Letting n, b and q be the number of elastic state variables, boundary conditions and inequality constraints and denoting the set of boundary conditions and inequality constraints by $\boldsymbol{\phi}$ and $\mathbf{c}$, respectively, the above mentioned dynamic optimization problems can be generally recast in a fictitious domain $\rho \in [-1,+1]$, related to the physical domain $r \in [R_{\mathrm{i}}, R_{\mathrm{o}}]$ by

$$r = \frac{R_{\mathrm{o}} - R_{\mathrm{i}}}{2}\rho + \frac{R_{\mathrm{o}} + R_{\mathrm{i}}}{2}, \tag{30}$$

as follows

$$\begin{aligned}
\min_{v(\rho)} \quad & \mathcal{J} = \mathcal{M}(R_{\mathrm{i}}, \mathbf{y}(-1), R_{\mathrm{o}}, \mathbf{y}(+1)) + \frac{R_{\mathrm{o}} - R_{\mathrm{i}}}{2} \int_{-1}^{+1} \mathcal{L}(\rho, \mathbf{y}(\rho), v(\rho))\, d\rho \\
\text{s.t.} \quad & \frac{d\mathbf{y}(\rho)}{d\rho} = \frac{R_{\mathrm{o}} - R_{\mathrm{i}}}{2} \mathbf{a}(\rho, \mathbf{y}(\rho), v(\rho)), \\
& \boldsymbol{\phi}(R_{\mathrm{i}}, \mathbf{y}(-1), R_{\mathrm{o}}, \mathbf{y}(+1)) = \mathbf{0}, \\
& \mathbf{c}(\rho, \mathbf{y}(\rho), v(\rho)) \le \mathbf{0},
\end{aligned} \tag{31}$$

where $\mathbf{a} : [-1,+1] \times \mathbb{R}^n \times \mathbb{R} \to \mathbb{R}^n$, $\mathcal{M} : \mathbb{R} \times \mathbb{R}^n \times \mathbb{R} \times \mathbb{R}^n \to \mathbb{R}$, $\mathcal{L} : [-1,+1] \times \mathbb{R}^n \times \mathbb{R} \to \mathbb{R}$, $\boldsymbol{\phi} : \mathbb{R} \times \mathbb{R}^n \times \mathbb{R} \times \mathbb{R}^n \to \mathbb{R}^b$ and $\mathbf{c} : [-1,+1] \times \mathbb{R}^n \times \mathbb{R} \to \mathbb{R}^q$ are functions whose regularity is at least sufficient to guarantee the existence of a numerical solution. Note that, in order to have a coherent and compact formulation of the discretized version, that will be explained below, $\mathbf{a}$, $\boldsymbol{\phi}$ and $\mathbf{c}$ are interpreted as row vector functions. The objective functional $\mathcal{J}$ is made up of two terms: $\mathcal{M}$ takes the name of *Mayer* cost and represents a punctual term of the elastic states at boundaries, while the integral term is called the *Lagrange* cost and it is a distributed cost associated with the whole domain.

Among numerical methods, the so-called "pseudospectral" ones have been gaining much interest and their theoretical development is

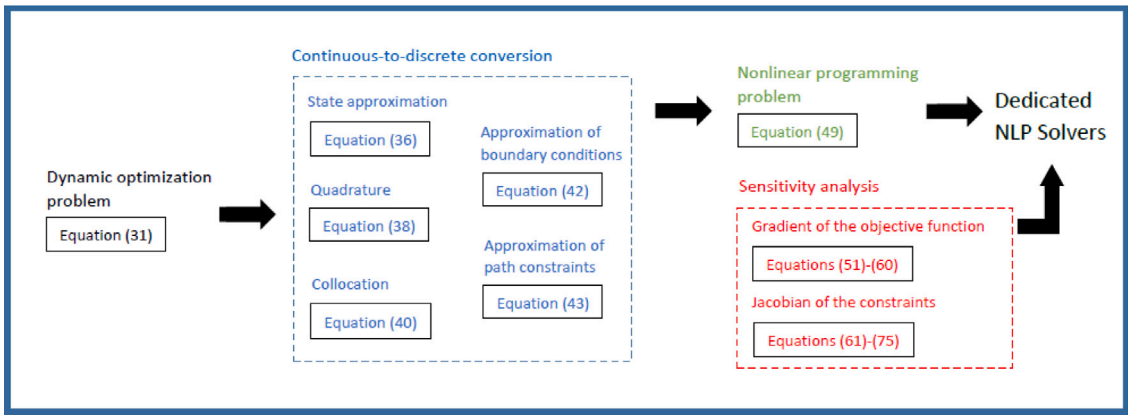

Fig. 3. A flowchart summarizing the transcription procedure and the sensitivity analysis.

more and more refined which, together with the increasing improvement of computers generation, led researchers to efficient algorithms to numerically solve dynamic optimization problems [37]. These methods permit the parameterization of the state and/or of the control function using specified functional forms and performing a procedure called "collocation" at chosen points called "nodes" [38]. More precisely, the trajectories of the state variables are approximated by polynomials and the differential equations are then discretized through a collocation procedure that makes use of particular nodes obtained from quadrature points [23]. In this way a dynamic optimization problem, whose solution has to be searched within an infinite-dimensional domain, is transcribed into a nonlinear programming problem. More recently, a great deal of research has been done in the class of pseudospectral methods whose collocation points are the roots of certain orthogonal polynomials (or a linear combination of their derivatives). For instance, collocation points can range from roots of Legendre–Gauss, Legendre–Gauss–Lobatto, Legendre–Gauss–Radau polynomials, and others (see, e.g., [39–41]). In this study, the application of the Legendre–Gauss–Radau (LGR) pseudospectral method to optimization problems concerning axisymmetric FGM bodies is presented. The transcription of the dynamic optimization problem into a finite-dimensional NLP problem (Section 4.2) and the associated sensitivity analysis (Section 4.3) are emphasized and summarized in Fig. 3. An application of the LGR pseudospectral method to dynamic optimization problems, though pertaining to another class of problems in mechanics, has been recently proposed in [42], where the shape of elastic straight beams for minimum mass under buckling requirements has been sought.

4.1. Employed notation

Hereinafter, all vector functions will be treated as row vectors, whereas any scalar vector is recast as a column vector. Moreover, if $\mathbf{f} : \mathbb{R}^k \to \mathbb{R}^l$ is a function that maps row vectors $\mathbf{p} \in \mathbb{R}^k$ to row vectors $\mathbf{f}(\mathbf{p}) \in \mathbb{R}^l$, then the result of evaluating $\mathbf{f}(\mathbf{p})$ at points $(\mathbf{p}_1, \mathbf{p}_2, \dots, \mathbf{p}_N)$ is the matrix $\mathbf{F} = [\mathbf{f}(\mathbf{p}_j)]_N^1$, namely

$$\mathbf{F} = [\mathbf{f}(\mathbf{p}_j)]_N^1 = \begin{bmatrix} \mathbf{f}(\mathbf{p}_1) \\ \mathbf{f}(\mathbf{p}_2) \\ \vdots \\ \mathbf{f}(\mathbf{p}_N) \end{bmatrix} \in \mathbb{R}^{N\times l}.$$

A single subscript i attached to a matrix $\mathbf{P} \in \mathbb{R}^{k\times l}$, i.e., $\mathbf{P}_i$, denotes the ith row of the matrix $\mathbf{P}$, whereas $\mathbf{P}_{i,j}$ denotes the (i,j)th element of the matrix $\mathbf{P}$. Moreover, the notation $\mathbf{P}_{:,j}$ will be used to denote the jth column of $\mathbf{P}$ and the notation $\mathbf{P}^\top$ will be used to denote the transpose of $\mathbf{P}$.

Next, let $\mathbf{P}$ and $\mathbf{Q}$ be $k \times l$ matrices. Then, the element-by-element multiplication of $\mathbf{P}$ and $\mathbf{Q}$ is defined as

$$\mathbf{P}\circ\mathbf{Q} = \begin{bmatrix} p_{11}q_{11} & p_{12}q_{12} & \cdots & p_{1l}q_{1l} \\ p_{21}q_{21} & p_{22}q_{22} & \cdots & p_{2l}q_{2l} \\ \vdots & \vdots & \ddots & \vdots \\ p_{k1}q_{k1} & p_{k2}q_{k2} & \cdots & p_{kl}q_{kl} \end{bmatrix}.$$

Note that $\mathbf{P}\circ\mathbf{Q}$ is not standard matrix multiplication. Furthermore, if $\mathbf{p} \in \mathbb{R}^k$, then the operation $\mathrm{diag}(\mathbf{p})$ denotes the $k \times k$ diagonal matrix formed by the element of $\mathbf{p}$, namely

$$\mathrm{diag}(\mathbf{p}) = \begin{bmatrix} p_1 & 0 & \cdots & 0 \\ 0 & p_2 & \cdots & 0 \\ \vdots & \vdots & \ddots & \vdots \\ 0 & 0 & \cdots & p_k \end{bmatrix}.$$

The notation for derivatives of functions of vectors is defined next. First, let $f(\mathbf{p})$ with $f : \mathbb{R}^k \to \mathbb{R}$. Then, the gradient of f with respect to $\mathbf{p}$ is a row vector of length k and defined as

$$\nabla_{\mathbf{p}} f(\mathbf{p}) = \begin{bmatrix} \frac{\partial f}{\partial p_1} & \frac{\partial f}{\partial p_2} & \cdots & \frac{\partial f}{\partial p_k} \end{bmatrix} \in \mathbb{R}^k.$$

Finally, let $\mathbf{f}(\mathbf{p})$ with $\mathbf{f} : \mathbb{R}^k \to \mathbb{R}^l$, where $\mathbf{p}$ may be either a row or column vector and $\mathbf{f}(\mathbf{p})$ has the same orientation (i.e., either row or column vector) as $\mathbf{p}$. Then, the Jacobian of $\mathbf{f}$ with respect to $\mathbf{p}$ is the $l \times k$ matrix whose ith row is $\nabla_{\mathbf{p}} f_i$, namely

$$\nabla_{\mathbf{p}}\mathbf{f} = \begin{bmatrix} \nabla_{\mathbf{p}} f_1 \\ \nabla_{\mathbf{p}} f_2 \\ \vdots \\ \nabla_{\mathbf{p}} f_l \end{bmatrix} = \begin{bmatrix} \frac{\partial f_1}{\partial p_1} & \frac{\partial f_1}{\partial p_2} & \cdots & \frac{\partial f_1}{\partial p_k} \\ \frac{\partial f_2}{\partial p_1} & \frac{\partial f_2}{\partial p_2} & \cdots & \frac{\partial f_2}{\partial p_k} \\ \vdots & \vdots & \ddots & \vdots \\ \frac{\partial f_l}{\partial p_1} & \frac{\partial f_l}{\partial p_2} & \cdots & \frac{\partial f_l}{\partial p_k} \end{bmatrix} \in \mathbb{R}^{l\times k}.$$

4.2. Continuous-to-discrete conversion

Suppose that the interval $[-1, +1]$ is divided into K sub-intervals $[\rho_{k-1}, \rho_k]$, $k = 1, 2, \dots, K$, where $\rho_0, \rho_1, \dots, \rho_K$ are the mesh points and $\rho_0 = -1$ and $\rho_K = +1$. Letting $\mathbf{y}^{(k)}(\rho)$ and $v^{(k)}(\rho)$ be the (row) vector functions containing elastic state variables and the control function in the kth interval, respectively, the objective functional $\mathcal{J}$ can be rewritten as

$$\mathcal{J} = \mathcal{M}(R_\mathrm{i}, \mathbf{y}(-1), R_\mathrm{o}, \mathbf{y}(+1)) + \frac{R_\mathrm{o} - R_\mathrm{i}}{2} \sum_{k=1}^{K} \int_{\rho_{k-1}}^{\rho_k} \mathcal{L}\left(\rho, \mathbf{y}^{(k)}(\rho), v^{(k)}(\rho)\right) d\rho. \tag{32}$$

As far as the differential and path constraints in the kth mesh interval are concerned, one can write

$$\frac{d\mathbf{y}^{(k)}(\rho)}{d\rho} = \frac{R_\mathrm{o} - R_\mathrm{i}}{2} \mathbf{a}\left(\rho, \mathbf{y}^{(k)}(\rho), v^{(k)}(\rho)\right) \tag{33}$$

and

$$\mathbf{c}\left(\rho, \mathbf{y}^{(k)}(\rho), v^{(k)}(\rho)\right) \leq \mathbf{0}, \tag{34}$$

respectively, whereas the boundary conditions may be recast as

$$\boldsymbol{\phi}\left(R_{\mathrm{i}}, \mathbf{y}^{(1)}(-1), R_{\mathrm{o}}, \mathbf{y}^{(K)}(+1)\right) = \mathbf{0}. \tag{35}$$

Moreover, because elastic state variables must be continuous at each interior mesh point, it is required also that the condition $\mathbf{y}^{(k)}(\rho_k^-) = \mathbf{y}^{(k)}(\rho_k^+)$ for $k = 1, \ldots, K-1$ be satisfied. To guarantee this latter condition, the following pseudospectral scheme based on the Legendre–Gauss–Radau (LGR) transcription process is adopted. In particular, let $\rho_1^{(k)}, \ldots, \rho_{N_k}^{(k)}$ denote the collocation points (defined below) in the kth sub-interval, let $\rho_{N_{k+1}}^{(k)}$ be the right endpoint of the sub-interval (noncollocated point), the (row) vector of elastic states in the kth sub-interval is approximated as

$$\mathbf{y}^{(k)}(\rho) \approx \mathbf{Y}^{(k)}(\rho) = \sum_{j=1}^{N_k+1} \mathbf{Y}_j^{(k)} \ell_j^{(k)}(\rho), \tag{36}$$

where $\mathbf{Y}_j^{(k)}$ $(j = 1, 2, \ldots, N_k)$ are the approximations of the state variables at the LGR points in mesh interval k, while $\ell_j^{(k)}$ is the jth Lagrange polynomial in the kth sub-interval which is defined by

$$\ell_j^{(k)}(\rho) = \prod_{l=1, l\neq j}^{N_k+1} \frac{\rho - \rho_l^{(k)}}{\rho_j^{(k)} - \rho_l^{(k)}},$$

where $(\rho_1^{(k)}, \rho_2^{(k)}, \ldots, \rho_{N_k}^{(k)})$ are the LGR collocation points in mesh interval k defined on the sub-interval $\rho \in [\rho_{k-1}, \rho_k]$. In particular, the LGR collocation points in mesh interval k are given by the roots of the polynomial $\mathcal{P}_{N_k-1} + \mathcal{P}_{N_k}$, where $\mathcal{P}_{N_k-1}$ and $\mathcal{P}_{N_k}$ are the Legendre polynomials of degree $N_k - 1$ and N_k, respectively.

Differentiating (36) with respect to ρ, one obtains

$$\frac{d\mathbf{Y}^{(k)}(\rho)}{d\rho} = \sum_{j=1}^{N_k+1} \mathbf{Y}_j^{(k)} \frac{d\ell_j^{(k)}(\rho)}{d\rho}. \tag{37}$$

Moreover, the objective functional of Eq. (32) is then approximated using a multiple interval LGR quadrature as

$$\mathcal{J} = \mathcal{M}\left(R_{\mathrm{i}}, \mathbf{Y}_1^{(1)}, R_{\mathrm{o}}, \mathbf{Y}_{N_K+1}^{(K)}\right) + \frac{R_{\mathrm{o}} - R_{\mathrm{i}}}{2} \sum_{k=1}^{K} \sum_{j=1}^{N_k} \omega_j^{(k)} \mathcal{L}\left(\rho_j^{(k)}, \mathbf{Y}_j^{(k)}, V_j^{(k)}\right), \tag{38}$$

where $\mathbf{Y}_1^{(1)}$ and $\mathbf{Y}_{N_K+1}^{(K)}$ are the approximations of $\mathbf{y}(-1)$ and $\mathbf{y}(+1)$, respectively, $\omega_j^{(k)}$ $(j = 1, 2, \ldots, N_k)$ are the LGR quadrature weights in the kth mesh interval, given by

$$\begin{cases} \omega_1^{(k)} = \dfrac{2}{N_k^2}, \\ \omega_i^{(k)} = \dfrac{1}{(1-\rho_i^{(k)})\left(\frac{d\mathcal{P}_{N_k-1}\left(\rho_i^{(k)}\right)}{d\rho}\right)^2}, \qquad (i = 2, 3, \ldots, N_k) \end{cases} \tag{39}$$

and $V_j^{(k)}$ $(j = 1, 2, \ldots, N_k)$ are the approximations of the metallic volume fraction at the N_k LGR points in the kth mesh interval.

Collocating the differential constraints of Eq. (33) at the N_k LGR points by means of (37), one obtains

$$\sum_{j=1}^{N_k+1} D_{ij}^{(k)} \mathbf{Y}_j^{(k)} - \frac{R_{\mathrm{o}} - R_{\mathrm{i}}}{2} \mathbf{a}\left(\rho_i^{(k)}, \mathbf{Y}_i^{(k)}, V_i^{(k)}\right) = \mathbf{0}, \qquad i = 1, 2, \ldots, N_k, \tag{40}$$

where

$$D_{ij}^{(k)} = \frac{d\ell_j^{(k)}\left(\rho_i^{(k)}\right)}{d\rho}, \quad i = 1, \ldots, N_k, \quad j = 1, \ldots, N_k + 1, \tag{41}$$

is the $N_k \times (N_k + 1)$ differentiation matrix in the kth mesh interval.

Next, the path constraint of Eq. (34) in the kth mesh interval are enforced at the N_k LGR points as

$$\mathbf{c}\left(\rho_i^{(k)}, \mathbf{Y}_i^{(k)}, V_i^{(k)}\right) \leq \mathbf{0}, \qquad i = 1, 2, \ldots, N_k. \tag{42}$$

Finally, the boundary conditions of Eq. (35) are approximated as

$$\boldsymbol{\phi}\left(R_{\mathrm{i}}, \mathbf{Y}_1^{(1)}, R_{\mathrm{o}}, \mathbf{Y}_{N_K+1}^{(K)}\right) = \mathbf{0}. \tag{43}$$

It is worth to notice that the continuity in the elastic state vector at the interior mesh points, enforced via the condition

$$\mathbf{Y}_{N_k+1}^{(k)} = \mathbf{Y}_1^{(k+1)}, \qquad k = 1, 2, \ldots, K-1, \tag{44}$$

is taken into account explicitly.

Introducing the notation

$$\boldsymbol{\rho}^{(k)} = \begin{bmatrix} \rho_1^{(k)} \\ \rho_2^{(k)} \\ \vdots \\ \rho_{N_k}^{(k)} \end{bmatrix}, \quad \mathbf{Y}^{(k)} = \begin{bmatrix} \mathbf{Y}_1^{(k)} \\ \mathbf{Y}_2^{(k)} \\ \vdots \\ \mathbf{Y}_{N_k}^{(k)} \end{bmatrix}, \quad k = 1, 2, \ldots, K-1,$$

$$\boldsymbol{\rho}^{(K)} = \begin{bmatrix} \rho_1^{(K)} \\ \rho_2^{(K)} \\ \vdots \\ \rho_{N_K+1}^{(K)} \end{bmatrix}, \quad \mathbf{Y}^{(K)} = \begin{bmatrix} \mathbf{Y}_1^{(K)} \\ \mathbf{Y}_2^{(K)} \\ \vdots \\ \mathbf{Y}_{N_K+1}^{(K)} \end{bmatrix},$$

$$\mathbf{V}^{(k)} = \begin{bmatrix} V_1^{(k)} \\ V_2^{(k)} \\ \vdots \\ V_{N_k}^{(k)} \end{bmatrix}, \quad \boldsymbol{\omega}^{(k)} = \begin{bmatrix} \omega_1^{(k)} \\ \omega_2^{(k)} \\ \vdots \\ \omega_{N_k}^{(k)} \end{bmatrix}, \quad \mathbf{L}^{(k)} = \begin{bmatrix} \mathcal{L}\left(\rho_1^{(k)}, \mathbf{Y}_1^{(k)}, V_1^{(k)}\right) \\ \mathcal{L}\left(\rho_2^{(k)}, \mathbf{Y}_2^{(k)}, V_2^{(k)}\right) \\ \vdots \\ \mathcal{L}\left(\rho_{N_k}^{(k)}, \mathbf{Y}_{N_k}^{(k)}, V_{N_k}^{(k)}\right) \end{bmatrix},$$

$$\mathbf{A}^{(k)} = \begin{bmatrix} \mathbf{a}\left(\rho_1^{(k)}, \mathbf{Y}_1^{(k)}, V_1^{(k)}\right) \\ \mathbf{a}\left(\rho_2^{(k)}, \mathbf{Y}_2^{(k)}, V_2^{(k)}\right) \\ \vdots \\ \mathbf{a}\left(\rho_{N_k}^{(k)}, \mathbf{Y}_{N_k}^{(k)}, V_{N_k}^{(k)}\right) \end{bmatrix}, \quad \mathbf{C}^{(k)} = \begin{bmatrix} \mathbf{c}\left(\rho_1^{(k)}, \mathbf{Y}_1^{(k)}, V_1^{(k)}\right) \\ \mathbf{c}\left(\rho_2^{(k)}, \mathbf{Y}_2^{(k)}, V_2^{(k)}\right) \\ \vdots \\ \mathbf{c}\left(\rho_{N_k}^{(k)}, \mathbf{Y}_{N_k}^{(k)}, V_{N_k}^{(k)}\right) \end{bmatrix},$$

$k = 1, 2, \ldots, K$

and letting

$$\boldsymbol{\rho} = \begin{bmatrix} \boldsymbol{\rho}^{(1)} \\ \boldsymbol{\rho}^{(2)} \\ \vdots \\ \boldsymbol{\rho}^{(K)} \end{bmatrix} \in \mathbb{R}^{N+1}, \quad \boldsymbol{\omega} = \begin{bmatrix} \boldsymbol{\omega}^{(1)} \\ \boldsymbol{\omega}^{(2)} \\ \vdots \\ \boldsymbol{\omega}^{(K)} \end{bmatrix} \in \mathbb{R}^{N}, \quad \mathbf{Y} = \begin{bmatrix} \mathbf{Y}^{(1)} \\ \mathbf{Y}^{(2)} \\ \vdots \\ \mathbf{Y}^{(K)} \end{bmatrix} \in \mathbb{R}^{(N+1)\times n},$$

$$\mathbf{V} = \begin{bmatrix} \mathbf{V}^{(1)} \\ \mathbf{V}^{(2)} \\ \vdots \\ \mathbf{V}^{(K)} \end{bmatrix} \in \mathbb{R}^{N}, \quad \mathbf{L} = \begin{bmatrix} \mathbf{L}^{(1)} \\ \mathbf{L}^{(2)} \\ \vdots \\ \mathbf{L}^{(K)} \end{bmatrix} \in \mathbb{R}^{N}, \quad \mathbf{A} = \begin{bmatrix} \mathbf{A}^{(1)} \\ \mathbf{A}^{(2)} \\ \vdots \\ \mathbf{A}^{(K)} \end{bmatrix} \in \mathbb{R}^{N\times n},$$

$$\mathbf{C} = \begin{bmatrix} \mathbf{C}^{(1)} \\ \mathbf{C}^{(2)} \\ \vdots \\ \mathbf{C}^{(K)} \end{bmatrix} \in \mathbb{R}^{N\times q},$$

where $N = \sum_{k=1}^{K} N_k$, the objective functional and discretized differential constraints given in Eqs. (38) and (40) can be written compactly as

$$\mathcal{J} = \mathcal{M}\left(R_{\mathrm{i}}, \mathbf{Y}_1, R_{\mathrm{o}}, \mathbf{Y}_{N+1}\right) + \frac{R_{\mathrm{o}} - R_{\mathrm{i}}}{2} \boldsymbol{\omega}^{\top} \mathbf{L} \tag{45}$$

and

$$\mathbf{D}\mathbf{Y} - \frac{R_{\mathrm{o}} - R_{\mathrm{i}}}{2} \mathbf{A} = \mathbf{0}, \tag{46}$$

where $\mathbf{D} \in \mathbb{R}^{N\times(N+1)}$ is the LGR differentiation matrix, which has a block structure with nonzero elements defined by the matrix given in Eq. (41). The extra column of $\mathbf{D}$ is due to the Lagrange polynomial

at the noncollocated point $\rho_{N+1} = 1$. Finally, the discretized path constraints of Eq. (42) and boundary conditions of Eq. (43) are expressed as

$$\mathbf{C} \leq \mathbf{0} \tag{47}$$

and

$$\boldsymbol{\phi}\left(R_{\mathrm{i}}, \mathbf{Y}_1, R_{\mathrm{o}}, \mathbf{Y}_{N+1}\right) = \mathbf{0}, \tag{48}$$

respectively. Hence, Eqs. (31) may be transcribed into the following NLP problem:

$$\begin{aligned} \min_{\mathbf{Y},\mathbf{V},R_{\mathrm{i}},R_{\mathrm{o}}} \quad & \mathcal{J} = \mathcal{M}\left(R_{\mathrm{i}}, \mathbf{Y}_1, R_{\mathrm{o}}, \mathbf{Y}_{N+1}\right) + \Omega \\ \text{s.t.} \quad & \boldsymbol{\Delta} = \mathbf{0}, \\ & \boldsymbol{\phi}\left(R_{\mathrm{i}}, \mathbf{Y}_1, R_{\mathrm{o}}, \mathbf{Y}_{N+1}\right) = \mathbf{0}, \\ & \mathbf{C} \leq \mathbf{0}, \end{aligned} \tag{49}$$

where $\Omega = \frac{R_{\mathrm{o}}-R_{\mathrm{i}}}{2}\boldsymbol{\omega}^{\top}\mathbf{L}$ and $\boldsymbol{\Delta} = \mathbf{D}\mathbf{Y} - \frac{R_{\mathrm{o}}-R_{\mathrm{i}}}{2}\mathbf{A}$. Eqs. (49) represent a finite-dimensional constrained NLP problem, whose decision variables are the approximation of the elastic states and the values of the metallic volume fraction at the LGR points.

4.3. Computation of sensitivities

The decision variables of the NLP problem (49) arising from the LGR pseudospectral method are the coordinates of the vector $\mathbf{z} \in \mathbb{R}^{N(n+1)+N+2}$ and aim at minimizing

$$f(\mathbf{z}) = \mathcal{M}(\mathbf{z}) + \Omega(\mathbf{z}) \tag{50}$$

subject to the constraint

$$\mathbf{h}(\mathbf{z}) \leq \mathbf{0},$$

where

$$\mathbf{z} = \begin{bmatrix} \mathbf{Y}_{:,1} \\ \mathbf{Y}_{:,2} \\ \vdots \\ \mathbf{Y}_{:,n} \\ \mathbf{V} \\ R_{\mathrm{i}} \\ R_{\mathrm{o}} \end{bmatrix}, \quad \mathbf{h} = \begin{bmatrix} \boldsymbol{\Delta}_{:,1} \\ \boldsymbol{\Delta}_{:,2} \\ \vdots \\ \boldsymbol{\Delta}_{:,n} \\ \mathbf{C}_{:,1} \\ \mathbf{C}_{:,2} \\ \vdots \\ \mathbf{C}_{:,q} \\ \boldsymbol{\phi}_{1:b} \end{bmatrix}.$$

Next, expressions for the gradient of the NLP objective function and the Jacobian of the NLP constraints are derived. Following [43], these NLP derivatives can be obtained by differentiating the functions of the original continuous dynamic optimization problem.

4.3.1. Gradient of the objective function

The gradient of the objective function (50) with respect to the LGR pseudospectral NLP decision vector $\mathbf{z}$ is given as

$$\nabla_{\mathbf{z}} f = \nabla_{\mathbf{z}}\mathcal{M} + \nabla_{\mathbf{z}}\Omega. \tag{51}$$

The derivative $\nabla_{\mathbf{z}}\mathcal{M}$ is obtained as

$$\nabla_{\mathbf{z}}\mathcal{M} = \begin{bmatrix} \nabla_{\mathbf{Y}}\mathcal{M} & \nabla_{\mathbf{V}}\mathcal{M} & \nabla_{R_{\mathrm{i}}}\mathcal{M} & \nabla_{R_{\mathrm{o}}}\mathcal{M} \end{bmatrix}, \tag{52}$$

where

$$\nabla_{\mathbf{Y}}\mathcal{M} = \begin{bmatrix} \nabla_{\mathbf{Y}_{:,1}}\mathcal{M} & \nabla_{\mathbf{Y}_{:,2}}\mathcal{M} & \dots & \nabla_{\mathbf{Y}_{:,n}}\mathcal{M} \end{bmatrix}, \quad \nabla_{\mathbf{V}}\mathcal{M} = \begin{bmatrix} \mathbf{0}_{1\times N} \end{bmatrix}. \tag{53}$$

The derivatives $\nabla_{\mathbf{Y}_{:,i}}\mathcal{M}$, $\nabla_{R_{\mathrm{i}}}\mathcal{M}$ and $\nabla_{R_{\mathrm{o}}}\mathcal{M}$ are obtained as

$$\nabla_{\mathbf{Y}_{:,i}}\mathcal{M} = \begin{bmatrix} \frac{\partial\mathcal{M}}{\partial y_i(R_{\mathrm{i}})} & \mathbf{0}_{1\times(N-1)} & \frac{\partial\mathcal{M}}{\partial y_i(R_{\mathrm{o}})} \end{bmatrix}, \quad i = 1, 2, \dots, n, \tag{54}$$

and

$$\nabla_{R_{\mathrm{i}}}\mathcal{M} = \frac{\partial\mathcal{M}}{\partial R_{\mathrm{i}}}, \quad \nabla_{R_{\mathrm{o}}}\mathcal{M} = \frac{\partial\mathcal{M}}{\partial R_{\mathrm{o}}}. \tag{55}$$

Next, $\nabla_{\mathbf{z}}\Omega$ is given as

$$\nabla_{\mathbf{z}}\Omega = \begin{bmatrix} \nabla_{\mathbf{Y}}\Omega & \nabla_{\mathbf{V}}\Omega & \nabla_{R_{\mathrm{i}}}\Omega & \nabla_{R_{\mathrm{o}}}\Omega \end{bmatrix}, \tag{56}$$

where

$$\nabla_{\mathbf{Y}}\Omega = \begin{bmatrix} \nabla_{\mathbf{Y}_{:,1}}\Omega & \nabla_{\mathbf{Y}_{:,2}}\Omega & \dots & \nabla_{\mathbf{Y}_{:,n}}\Omega \end{bmatrix}. \tag{57}$$

The derivatives $\nabla_{\mathbf{Y}_{:,i}}\Omega$, $\nabla_{\mathbf{V}}\Omega$, $\nabla_{R_{\mathrm{i}}}\Omega$ and $\nabla_{R_{\mathrm{o}}}\Omega$ are obtained as

$$\nabla_{\mathbf{Y}_{:,i}}\Omega = \begin{bmatrix} \frac{R_{\mathrm{o}}-R_{\mathrm{i}}}{2}\left\{\mathbf{w}\circ\left[\frac{\partial\mathcal{L}}{\partial y_i}\right]_N^1\right\}^{\top} & 0 \end{bmatrix}, \quad i = 1, 2, \dots, n, \tag{58}$$

$$\nabla_{\mathbf{V}}\Omega = \frac{R_{\mathrm{o}}-R_{\mathrm{i}}}{2}\left\{\mathbf{w}\circ\left[\frac{\partial\mathcal{L}}{\partial \upsilon}\right]_N^1\right\}^{\top}, \tag{59}$$

$$\nabla_{R_{\mathrm{i}}}\Omega = -\frac{1}{2}\mathbf{w}^{\top}\mathbf{L}, \quad \nabla_{R_{\mathrm{o}}}\Omega = \frac{1}{2}\mathbf{w}^{\top}\mathbf{L}. \tag{60}$$

It is shown from Eqs. (51)–(60) that the computation the objective function gradient requires that the first derivatives of $\mathcal{L}$ be determined with respect to the continuous states $\mathbf{y}$ and the control function υ, whereas the first derivatives of $\mathcal{M}$ be determined with respect to $\mathbf{y}(R_{\mathrm{i}})$, $\mathbf{y}(R_{\mathrm{o}})$, R_{i} and R_{o}. Furthermore, these derivatives are computed at either the N collocation points or at the endpoints.

4.3.2. Constraints Jacobian

The Jacobian of the constraints is defined as

$$\nabla_{\mathbf{z}}\mathbf{h} = \begin{bmatrix} \nabla_{\mathbf{z}}\boldsymbol{\Delta}_{:,1} \\ \nabla_{\mathbf{z}}\boldsymbol{\Delta}_{:,2} \\ \vdots \\ \nabla_{\mathbf{z}}\boldsymbol{\Delta}_{:,n} \\ \nabla_{\mathbf{z}}\mathbf{C}_{:,1} \\ \nabla_{\mathbf{z}}\mathbf{C}_{:,2} \\ \vdots \\ \nabla_{\mathbf{z}}\mathbf{C}_{:,q} \\ \nabla_{\mathbf{z}}\boldsymbol{\phi}_1 \\ \nabla_{\mathbf{z}}\boldsymbol{\phi}_2 \\ \vdots \\ \nabla_{\mathbf{z}}\boldsymbol{\phi}_b \end{bmatrix}. \tag{61}$$

The first derivatives of the defect constraints are obtained by

$$\nabla_{\mathbf{z}}\boldsymbol{\Delta}_{:,l} = \begin{bmatrix} \nabla_{\mathbf{Y}}\boldsymbol{\Delta}_{:,l} & \nabla_{\mathbf{V}}\boldsymbol{\Delta}_{:,l} & \nabla_{R_{\mathrm{i}}}\boldsymbol{\Delta}_{:,l} & \nabla_{R_{\mathrm{o}}}\boldsymbol{\Delta}_{:,l} \end{bmatrix}, \quad l = 1, 2, \dots, n, \tag{62}$$

where

$$\nabla_{\mathbf{Y}}\boldsymbol{\Delta}_{:,l} = \begin{bmatrix} \nabla_{\mathbf{Y}_{:,1}}\boldsymbol{\Delta}_{:,l} & \nabla_{\mathbf{Y}_{:,2}}\boldsymbol{\Delta}_{:,l} & \dots & \nabla_{\mathbf{Y}_{:,n}}\boldsymbol{\Delta}_{:,l} \end{bmatrix}. \tag{63}$$

The derivatives $\nabla_{\mathbf{Y}_{:,i}}\boldsymbol{\Delta}_{:,l}$, $\nabla_{\mathbf{V}}\boldsymbol{\Delta}_{:,l}$, $\nabla_{R_{\mathrm{i}}}\boldsymbol{\Delta}_{:,l}$ and $\nabla_{R_{\mathrm{o}}}\boldsymbol{\Delta}_{:,l}$ (with $l = 1, 2, \dots, n$) are obtained as

$$\nabla_{\mathbf{Y}_{:,i}}\boldsymbol{\Delta}_{:,l} = \begin{bmatrix} \delta_{il}\mathbf{D}_{:,1:N} - \frac{R_{\mathrm{o}}-R_{\mathrm{i}}}{2}\mathrm{diag}\left(\left[\frac{\partial a_l}{\partial y_i}\right]_N^1\right) & \delta_{il}\mathbf{D}_{:,N+1} \end{bmatrix}, \tag{64}$$

$i = 1, 2, \dots, n,$

where δ_{il} is the Kronecker delta function, and

$$\nabla_{\mathbf{V}}\boldsymbol{\Delta}_{:,l} = -\frac{R_{\mathrm{o}}-R_{\mathrm{i}}}{2}\mathrm{diag}\left(\left[\frac{\partial a_l}{\partial \upsilon}\right]_N^1\right), \tag{65}$$

$$\nabla_{R_{\mathrm{i}}}\boldsymbol{\Delta}_{:,l} = \frac{1}{2}[a_l]_N^1, \quad \nabla_{R_{\mathrm{o}}}\boldsymbol{\Delta}_{:,l} = -\frac{1}{2}[a_l]_N^1. \tag{66}$$

As far as the derivatives of the inequality constraints are concerned, one may write

$$\nabla_{\mathbf{z}}\mathbf{C}_{:,e} = \begin{bmatrix} \nabla_{\mathbf{Y}}\mathbf{C}_{:,e} & \nabla_{\mathbf{V}}\mathbf{C}_{:,e} & \mathbf{0}_{N\times 1} & \mathbf{0}_{N\times 1} \end{bmatrix}, \quad e = 1, 2, \dots, q, \tag{67}$$

where

$$\nabla_{\mathbf{Y}}\mathbf{C}_{:,e} = \begin{bmatrix} \nabla_{\mathbf{Y}_{:,1}}\mathbf{C}_{:,e} & \nabla_{\mathbf{Y}_{:,2}}\mathbf{C}_{:,e} & \dots & \nabla_{\mathbf{Y}_{:,n}}\mathbf{C}_{:,e} \end{bmatrix}, \tag{68}$$

where the derivatives $\nabla_{\mathbf{Y}_{:,i}}\mathbf{C}_{:,e}$ and $\nabla_{\mathbf{V}}\mathbf{C}_{:,e}$ (with $e = 1, 2, \dots, q$) are given by

$$\nabla_{\mathbf{Y}_{:,i}}\mathbf{C}_{:,e} = \begin{bmatrix} \mathrm{diag}\left(\left[\frac{\partial c_e}{\partial y_i}\right]\right) & \mathbf{0}_{N\times 1} \end{bmatrix} \quad i = 1, 2, \dots, n, \tag{69}$$

and

$$\nabla_{\mathbf{V}}\mathbf{C}_{:,e} = \mathrm{diag}\left(\left[\frac{\partial c_e}{\partial v}\right]\right), \tag{70}$$

respectively. Finally, the first derivative of the boundary conditions are given as

$$\nabla_{\mathbf{z}}\phi_d = \left[\nabla_{\mathbf{Y}}\phi_d \quad \nabla_{\mathbf{V}}\phi_d \quad \nabla_{R_\mathrm{i}}\phi_d \quad \nabla_{R_\mathrm{o}}\phi_d\right], \quad d = 1, 2, \dots, b, \tag{71}$$

where

$$\nabla_{\mathbf{Y}}\phi_d = \left[\nabla_{\mathbf{Y}_{:,1}}\phi_d \quad \nabla_{\mathbf{Y}_{:,2}}\phi_d \quad \dots \quad \nabla_{\mathbf{Y}_{:,n}}\phi_d\right] \tag{72}$$

and

$$\nabla_{\mathbf{V}}\phi_d = \left[\mathbf{0}_{1\times N}\right]. \tag{73}$$

The derivatives $\nabla_{\mathbf{Y}_{:,i}}\phi_d$, $\nabla_{R_\mathrm{i}}\phi_d$ and $\nabla_{R_\mathrm{o}}\phi_d$ (with $d = 1, 2, \dots, b$) are given by

$$\nabla_{\mathbf{Y}_{:,i}}\phi_d = \left[\frac{\partial\phi_d}{\partial y_i(R_\mathrm{i})} \quad \mathbf{0}_{1\times(N-1)} \quad \frac{\partial\phi_d}{\partial y_i(R_\mathrm{o})}\right], \quad i = 1, 2, \dots, n, \tag{74}$$

and

$$\nabla_{R_\mathrm{i}}\phi_d = \frac{\partial\phi_d}{\partial R_\mathrm{i}}, \quad \nabla_{R_\mathrm{o}}\phi_d = \frac{\partial\phi_d}{\partial R_\mathrm{o}}. \tag{75}$$

Also here, it is shown from Eqs. (61)–(75) that the NLP constraint Jacobian requires that the first derivatives of **c** and **a** with respect to the continuous states **y** and the control function v, whereas the derivatives of $\boldsymbol{\phi}$ are determined with respect to R_i, R_o, $\mathbf{y}(R_\mathrm{i})$ and $\mathbf{y}(R_\mathrm{o})$. Moreover, these derivatives are computed at either the N collocation points or at the endpoints.

5. Results and discussion

In this section, Problems 1–5 are solved by means of the numerical method described above. The transcription process has been performed by ad-hoc routines and a dedicated NLP solver has been employed to numerically solve the optimization problem. In all the simulations presented here, the termination tolerance on the first-order optimality and the termination tolerance on the decision variables are set to be 10^{-9}. The two bulk materials are steel and alumina, whose Young's moduli are taken to be $E_\mathrm{c} = 3.9\times10^5$ MPa and $E_\mathrm{m} = 2.1\times10^5$ MPa, respectively, and whose Poisson's ratios are $\nu_\mathrm{c} = 0.25$ and $\nu_\mathrm{m} = 0.33$, respectively.

5.1. Numerical solutions

Firstly, a comparison of numerical results for Problem 1 with results in [21] is made, namely when the Poisson's ratio is assumed uniform ($\nu = 1/3$), for $p_\mathrm{i} = 10$ MPa and for $R_\mathrm{i} = 20$ mm and $R_\mathrm{o} = 30$ mm, where necessary conditions for optimality under the single switching point assumption led to closed-form solutions. Figs. 4(a) and 4(b) forecast the numerical optimal solutions for the rate of change of the ceramic volume fraction and the corresponding ceramic volume fraction, respectively. It is clearly shown the existence of one switching point only, sharply identifiable as the number of mesh points increases. In particular, it is shown that the optimal solution is the one that first takes the value v_+ and then the value v_-, whereas the other solution must be discarded.

Letting $\mathrm{v}_+ = -0.02$, numerical optimal solutions have been forecast for different values of $\mathrm{v}_-/\mathrm{v}_+ = 10, 20, 30$ and of $R_\mathrm{o}/R_\mathrm{i}$, showing a good agreement with the locus of the switching point $\widetilde{r}$ reported in Eq. (15), as shown in Fig. 5(a) and commending the analytical approach adopted in [21]. Given the number of mesh intervals K and based on the symbols $\delta_1^{(K)}$ and $\delta_2^{(K)}$ defined in Fig. 4(a), one can define a parameter associated with the solution error with respect to the bang–bang solution as

$$\delta^{(K)} = \max\{\delta_1^{(K)}, \delta_2^{(K)}\}. \tag{76}$$

Table 2
Normalized maximum equivalent stress $\sigma^{\mathrm{T}}_{\mathrm{eq,max}}/p_\mathrm{i}$ associated with the optimal numerical solutions for both plane stress (Problem 2) and plane strain (Problem 3) load conditions.

	$R_\mathrm{o}/R_\mathrm{i}$	Uniform ν	Variable ν	
		Voigt & Reuss	Voigt	Reuss
Problem 2	1.50	2.64784	2.63510	2.63387
	1.75	2.13238	2.10822	2.10721
	2.00	1.90812	1.87851	1.87790
	2.25	1.78525	1.75261	1.75230
	2.50	1.70891	1.67442	1.67431
Problem 3	1.50	3.00000	3.00000	3.00168
	1.75	2.35846	2.36016	2.35536
	2.00	2.08191	2.07584	2.07400
	2.25	1.92205	1.90984	1.90848
	2.50	1.82429	1.80700	1.80613

Such definition is practical as it gives an immediate idea on the error on the locus of the switching point $\widetilde{r}$ reported in Eq. (15), rather than the conventional L_∞-norm errors defined on the whole radial interval. Fig. 5(b) shows that such error measure decreases as the mesh intervals K and the number of LGR points in each interval N_k increase.

Finally, Figs. 6(a) and 6(b) report the agreement found to exist between elastic stresses associated with the optimal volume fractions and those obtained by performing a finite element analysis for $R_\mathrm{o}/R_\mathrm{i} = 1.5$ and for both rules of mixture.

Critical remarks reported in Section 3.1.3 conveyed to the formulation of Problems 2 and 3, whose solutions are hardly tractable from the analytical viewpoint. Hence, the proposed numerical procedure is used. Solutions along the radial direction are computed until a marginal difference is obtained among successive iterations. The exponent $\mathcal{P}$ was taken to be equal to 60 in all the simulations. As before, solutions are firstly computed for a constant Poisson's ratio ($\nu = 1/3$), just to make a comparison with results for Problem 1, without the inclusion of the constraint on the rate of change of volume fractions (as before, the internal pressure is $p_\mathrm{i} = 10$ MPa). As shown in Figs. 7(a)–7(d) optimal metallic volume fractions for both Voigt and Reuss models and for both load conditions are numerically computed with $N_k = 10$ and $K = 9$. As shown in these figures, and unlike the stress formulation, the mixed formulation goes beyond the limits on the maximum and minimum derivatives of volume fractions, where the material partly grades throughout the radial coordinate.

As $R_\mathrm{o}/R_\mathrm{i}$ increases, forecast show that numerical solutions behave similarly in both plane state conditions, namely there is a finite interval between R_i and R_o where the material grades, while it is homogeneous elsewhere. In particular, there are initial and final radial strips where the optimal distribution of the material yields metallic ($V_\mathrm{m} = 1$) and ceramic ($V_\mathrm{m} = 0$) phases, respectively. The position of these radial strips depends on the geometric aspect of the cylinder. Specifically, the radial interval where the material grades decreases as the aspect ratio $R_\mathrm{o}/R_\mathrm{i}$ increases, being fixed the load condition. Numerical solutions for the normalized maximum equivalent Tresca stress $\sigma^{\mathrm{T}}_{\mathrm{eq,max}}/p_\mathrm{i}$, which still occur at the inner radius, have been reported in Table 2, where it is shown they are identical for Voigt and Reuss rules of mixture as well as lower than those associated with the Pontryagin's best extremal obtained from the stress formulation (approximately 34% for $R_\mathrm{o}/R_\mathrm{i} = 1.5$, if compared with the maximum equivalent stress shown in Figs. 6(a) and 6(b)).

Next, the variation of the Poisson's ratio is taken into account. The corresponding optimal solutions have been computed and reported in Table 2 for different aspect ratios. It is emphasized that numerical solutions do not remarkably differ from those associated with the uniform Poisson's ratio. This is due to the marginal variation between optimal metallic volume fractions for both cases (see Figs. 7(e) and 7(f), where optimal volume fractions have been computed for $R_\mathrm{o}/R_\mathrm{i} = 2$).

Eventually, as far as pressurized hollow spheres (Problem 4) and freely rotating hollow disks (Problem 5) are concerned, numerical

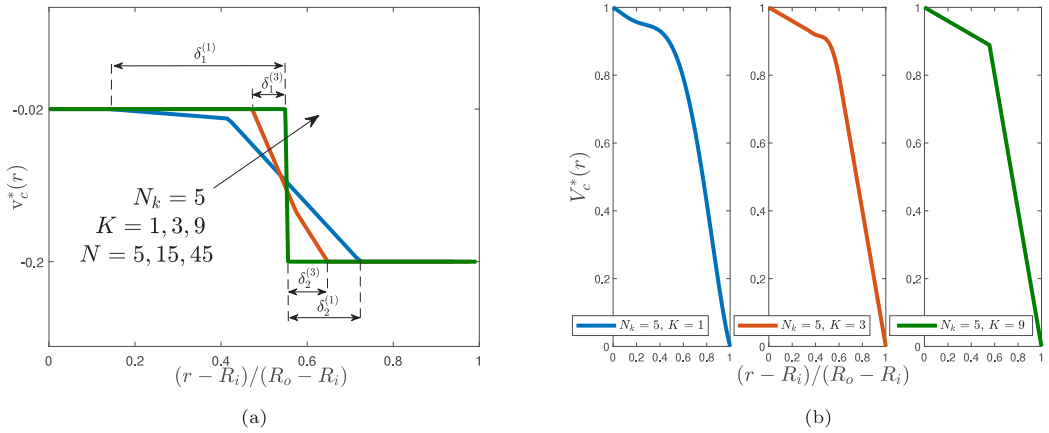

Fig. 4. Numerical optimal solutions of (a) the rate of change $v_c^*(r)$ and (b) the ceramic volume fraction $V_c^*(r)$ for $R_o/R_i = 1.5$ with different mesh points N_k along the radial coordinate (Problem 1).

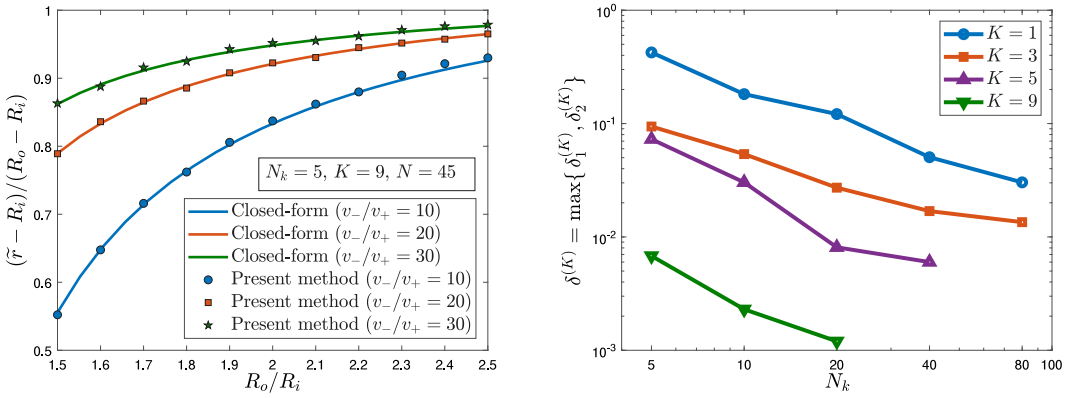

Fig. 5. (a) Analytical and numerical locus of the switching points for $v_-/v_+ = 10, 20, 30$ and for different instance of the aspect ratio R_o/R_i (Problem 1). (b) Solution error $\delta^{(K)}$ defined according to Eq. (76) vs. the number of LGR points in each segment N_k (Problem 1).

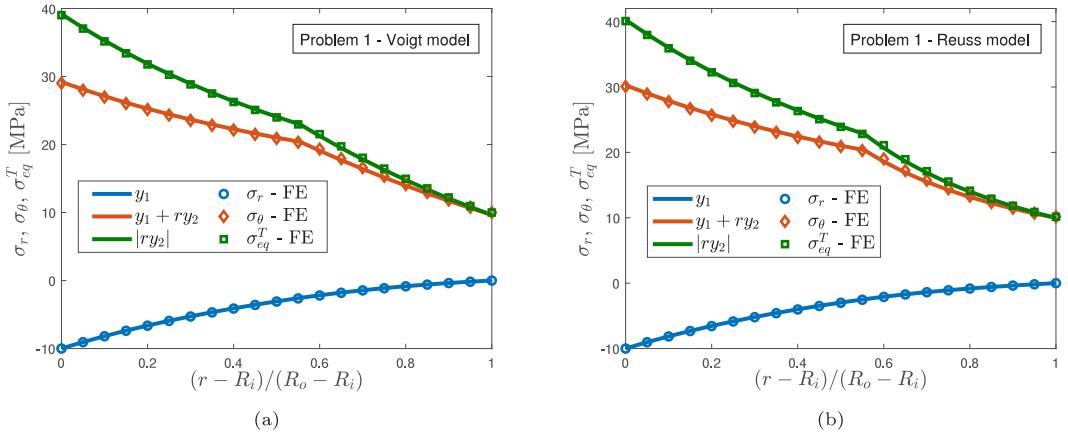

Fig. 6. Finite element validation of occurring stresses associated with the optimal numerical ceramic volume fractions for (a) Voigt and (b) Reuss models for a plane stress load condition (Problem 1) and for $p_i = 10$ MPa and $R_o/R_i = 1.5$.

solutions show similar behavior as the one previously reported for the cylinder, namely the presence of both radial homogeneous strips as well as subintervals where the material grades continuously from the metallic to the ceramic phase. Numerical values for ρ_m, ρ_c and ϖ have been taken as $7.8{\times}10^3$ kg/m^3, $3.9{\times}10^3$ kg/m^3 and 500 rad/s, respectively [5]. The corresponding optimal metallic volume fractions are shown in Figs. 8(a) and 8(b), respectively. Besides the free–free (FF) boundary condition, other boundary conditions associated with the rotating hollow disk problem have been also addressed by simply imposing different boundary conditions on y_1 and y_2 (see Figs. 8(c) and 8(d) for the free–clamped (FC) and clamped-clamped (CC) disks, respectively). It is worth noting how far the optimal solutions behavior is from the property variations commonly employed in the literature, as briefly reported in the following section.

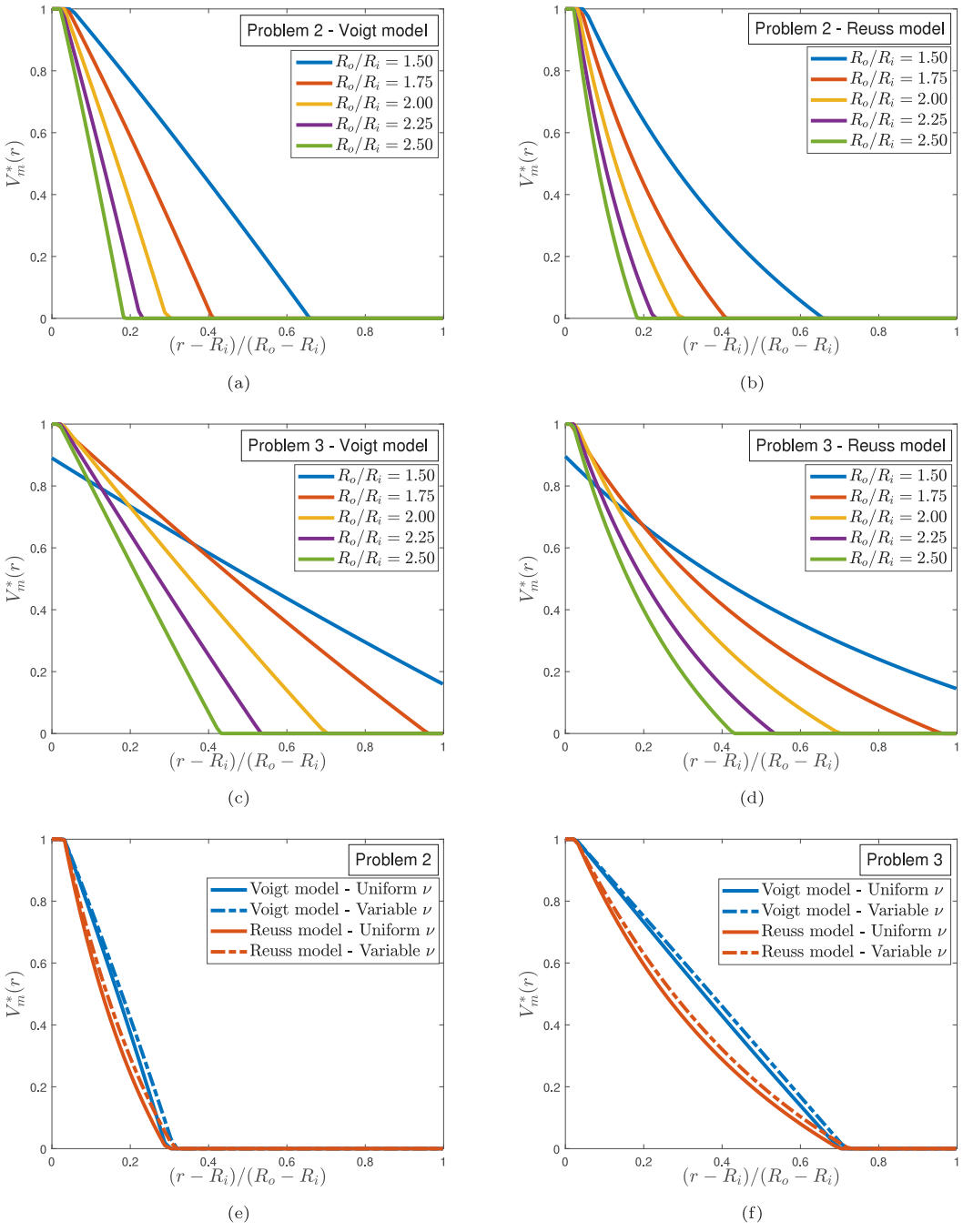

Fig. 7. Numerical optimal solutions for the metallic volume fraction for (a, c) Voigt and (b, d) Reuss models for the (a, b) plane stress and the (c, d) plane strain conditions and for different values of R_o/R_i. Effect of the variation of Poisson's ratio ν on the numerical optimal solutions for metallic volume fractions for Voigt and Reuss models, for the (e) plane stress and (f) plane strain conditions and for $R_o/R_i = 2$.

5.2. Comparison with the literature

For the sake of comparison with the literature, the mechanical behavior of functionally graded cylinders has been forecast by an finite element model considering a power gradation law, namely

$$\begin{cases} V_c^{[M\to C]}(r) = \left(\frac{r-R_i}{R_o-R_i}\right)^{\mu}, \\ V_c^{[C\to M]}(r) = 1 - \left(\frac{r-R_i}{R_o-R_i}\right)^{\mu}, \end{cases} \tag{77}$$

where μ is the grading index and notations $[C \to M]$ and $[M \to C]$ refer to having a ceramic material at the inner boundary and a metallic material at the outer boundary and viceversa, respectively. Numerical values for the associated normalized maximum Tresca stress have been reported in Table 3 for different values of μ and R_o/R_i. After a first examination of these values, it is straightforward to justify why $V_m > 0$ as $r \to R_i$, as computed stresses for $[C \to M]$ structures yield higher stresses. This is most probably the reason why a metallic homogeneous annular ring at the inner boundary is present in the overwhelming cases (see Figs. 7(a)–11(c)). A comparison between values in Tables 2 and 3 thus reflects the success of the applied approach, albeit some power-law volume fractions could lead to lower stresses for Problem 3 (see bold numerical values in Table 3). This apparent paradox is easily solved by the following considerations. As far as $[M \to C]$ structures are concerned, Fig. 9 shows elastic stresses that have been forecast for an internally pressurized cylinder in a plane strain condition with linear volume fractions ($\mu = 1$) and taking into consideration Voigt

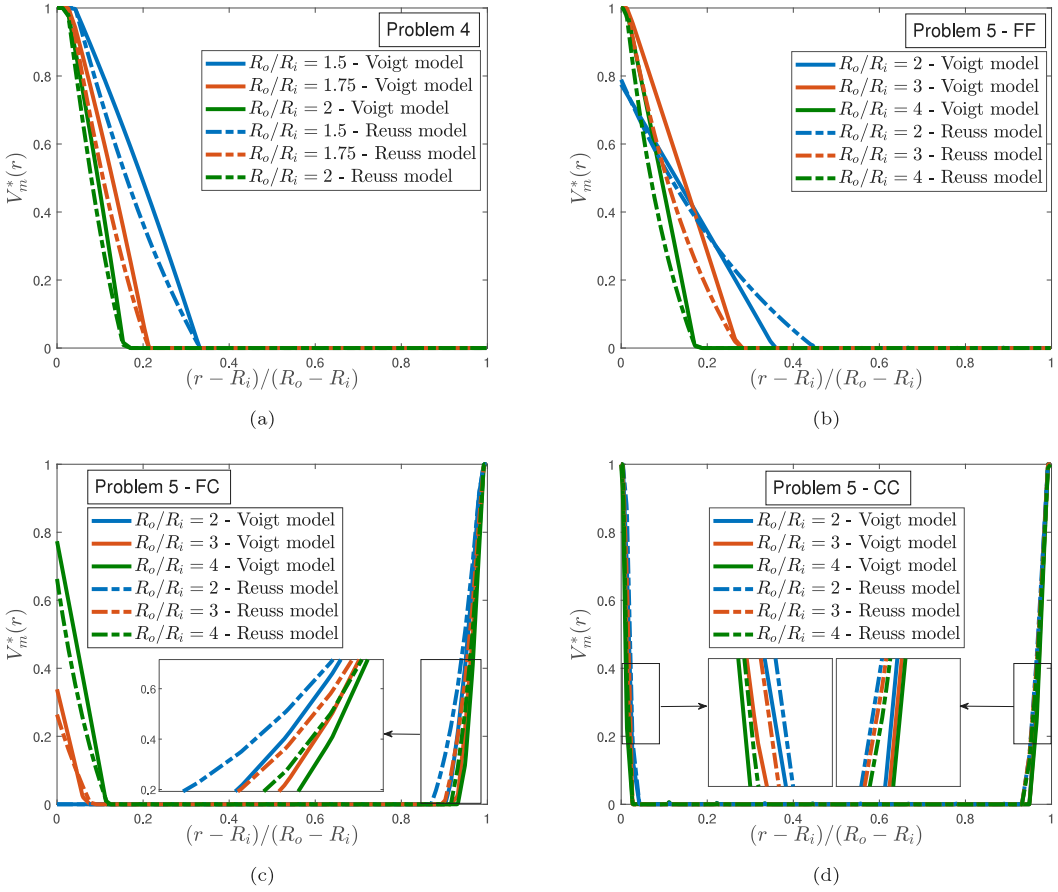

Fig. 8. Numerical optimal solutions for the metallic volume fraction for (a) internally pressurized spheres (Problem 4), (b) free–free (FF), (c) free–clamped (FC) and (d) clamped-clamped (CC) rotating hollow disks (Problem 5) for different values of R_o/R_i.

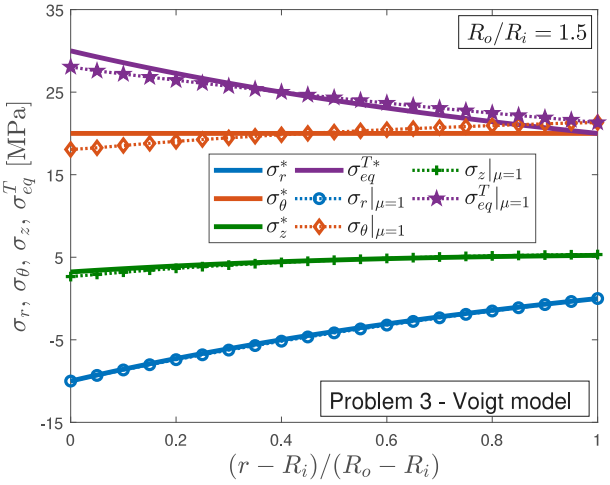

Fig. 9. Elastic stresses in an internally pressurized cylinder in a plane strain condition associated with linear volume fractions ($\mu = 1$) and compared to those associated with optimal solutions for Problem 3 ($R_o/R_i = 1.5$, Voigt model).

model. It is worth noting that the associated maximum value of the hoop stress, which is the objective functional in Problem 3, is higher than the one associated with the optimal volume fraction (see Fig. 7(c)), thus confirming the results found by the present approach. On the other hand, as far as $[C \to M]$ structures are concerned, it is interesting to plot the rate of change of the ceramic volume fraction $V_c^{[C\to M]}$, namely

$$\mathrm{v_c}(r) = \frac{d}{dr} V_c^{[C\to M]}(r) = \frac{-\mu}{R_o - R_i} \left(\frac{r - R_i}{R_o - R_i} \right)^{\mu - 1}, \tag{78}$$

as it has been done for different instance of the grading factor μ in Fig. 10(a), alongside with bounds $\mathrm{v}_- = -0.2$ and $\mathrm{v}_+ = -0.02$. The associated normalized equivalent stresses are shown in Fig. 10(b). The reason why the elastic equivalent stress associated with $\mu = 3$ is lower than the optimal one might stem from the violation of both the lower and upper constraints v_- and v_+ in different zones along the cylinder thickness with respect to the other volume fractions. In fact, if v_- becomes -0.4, namely $\mathrm{v}_-/\mathrm{v}_+ = 20$, normalized maximum equivalent stresses diminish below the bold values reported in Table 3 (for comparison, see [21]).

5.3. Additional results

For brevity, the following considerations are addressed only for the cylinder. Without loss of generality, numerical solutions have been computed for an aspect ratio $R_o/R_i = 2$.

5.3.1. Effect of external pressure

The effect of the external pressure on optimal solutions is now discussed. In the formulations of Problems 2 and 3, this can be accounted for by imposing $y_2(R_o) = -p_o$, where p_o is the value of such pressure. Numerical optimal solutions for different ratios p_o/p_i are shown in Figs. 11(a) and 11(b). Forecasts have been carried out by employing a variable Poisson's ratio along the radial coordinate.

As it is shown, the presence of the radial homogeneous strips may or may not take place, depending on the employed rule of mixture

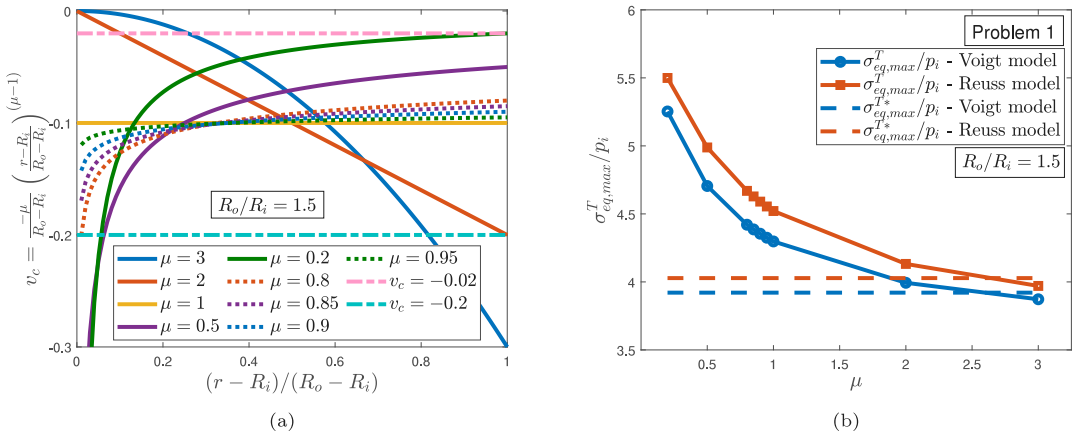

Fig. 10. (a) The rate of change of the ceramic volume fraction (78) for different instances of the grading factor μ and (b) the associated normalized maximum equivalent stresses.

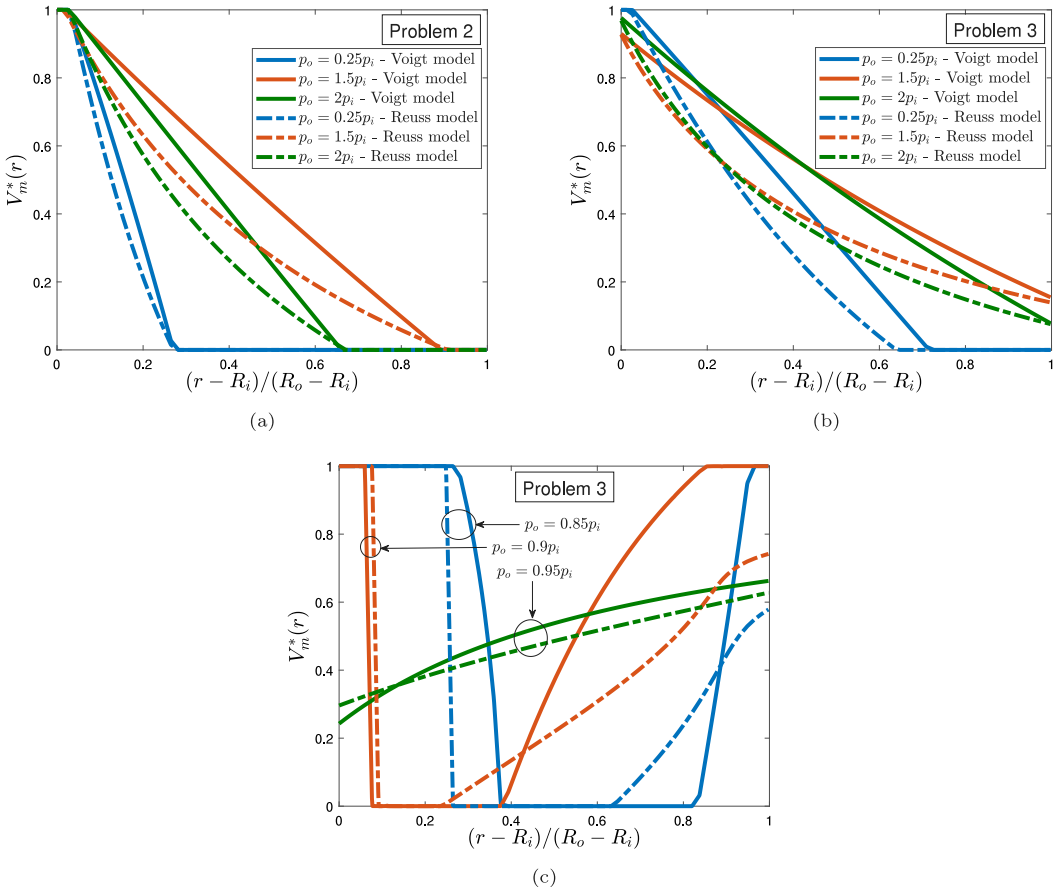

Fig. 11. Effect of the external pressure on the numerical optimal solutions for metallic volume fractions for Voigt and Reuss models, for the (a) plane stress (Problem 2) and (b, c) the plane strain (Problem 3) conditions and for $R_o/R_i = 2$.

and applied pressure ratio at the internal and external boundaries. Radial strips are not found to be necessarily at boundaries, for instance Fig. 11(c) shows numerical optimal volume fractions for Problem 3 for pressure ratios p_o/p_i increasingly tending to unity, where radial homogeneous strips can occur at several subintervals along the thickness, leading to the fully homogeneous distribution as a best strategy for the case p_o/p_i equal to 1 identically.

5.3.2. Inclusion of other micromechanical models

In the previous analyses, reference has been made to rules of mixtures only as micromechanical models, though these estimates could or could not provide upper and lower bounds for these properties. In fact, while the effective Young's modulus is bounded to those estimated by Voigt and Reuss models [44], Poisson's ratio might not [45]. A critical overview of different micromechanical models for the effective properties estimation could be found in [46] and more recently in [47,48]. These models include, but are not limited to, Hashin–Shtrikman upper and lower bounds, the Mori–Tanaka scheme and the self-consistent method [1]. Among all these models, the last one is not explicit, i.e. effective properties and volume fractions are nonlinearly coupled, requiring one to solve an additional subproblem at each iteration. Nevertheless, the present approach can easily include these requirements. For the sake of example, Figs. 12(a) and 12(b) show the optimal effective properties by considering each model in the case

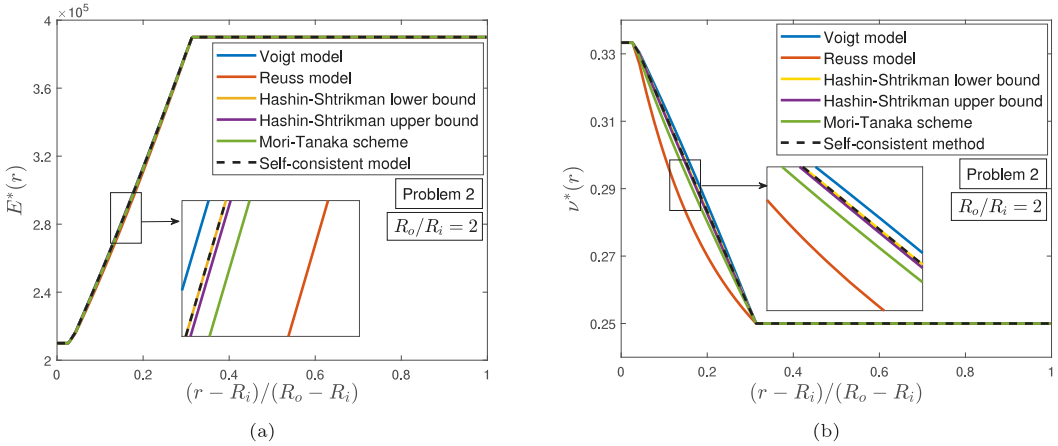

Fig. 12. Optimal variation of (a) Young's modulus and (b) Poisson's ratio for an internally pressurized cylinder in a plane stress load condition (Problem 2) and $R_o/R_i = 2$.

Table 3
Normalized maximum equivalent stress $\sigma^{T}_{eq,max}/p_i$ associated with the numerical solutions corresponding to the power gradation law (77) for both plane stress (Problem 2) and plane strain (Problem 3) conditions.

		R_o/R_i	$[M \to C]$		$[C \to M]$	
			Voigt	Reuss	Voigt	Reuss
Problem 2	$\mu = 3$	1.50	3.18459	3.27508	**3.88885**	**3.98321**
		2.00	2.44731	2.49749	2.81271	2.86198
		2.50	2.23278	2.26789	2.47629	2.50948
	$\mu = 2$	1.50	3.05397	3.16432	4.01505	4.14888
		2.00	2.36460	2.43003	2.88425	2.95764
		2.50	2.16854	2.21707	2.52776	2.57938
	$\mu = 1$	1.50	2.80599	2.93737	4.32988	4.54603
		2.00	2.18976	2.27747	3.07702	3.20747
		2.50	2.01935	2.09177	2.67616	2.77600
	$\mu = 0.5$	1.50	2.84333	2.82359	4.74929	5.02355
		2.00	2.10646	2.14041	3.35564	3.53660
		2.50	1.90513	1.93976	2.90586	3.05514
	$\mu = 0.2$	1.50	3.09066	2.98965	5.30944	5.54768
		2.00	2.26923	2.21266	3.75463	3.92537
		2.50	2.03139	1.98925	3.25344	3.40394
Problem 3	$\mu = 3$	1.50	3.19810	3.29516	**3.87238**	**3.97043**
		2.00	2.44904	2.50353	2.80653	2.85791
		2.50	2.23164	2.27006	2.47313	2.50782
	$\mu = 2$	1.50	3.06468	3.18416	3.99343	4.13227
		2.00	2.36157	2.43333	2.87698	2.95351
		2.50	2.16246	2.21612	2.52458	2.57857
	$\mu = 1$	1.50	**2.80653**	**2.95047**	4.29751	4.52119
		2.00	2.17315	2.27037	3.06910	3.20525
		2.50	1.99908	2.07988	2.67498	2.77965
	$\mu = 0.5$	1.50	**2.85201**	**2.82979**	4.70511	4.98849
		2.00	2.09001	2.12755	3.34956	3.53875
		2.50	1.88480	1.91969	2.91025	3.06723
	$\mu = 0.2$	1.50	3.09868	**2.99223**	5.25299	5.49933
		2.00	2.26268	2.20244	3.75463	3.93365
		2.50	2.02228	1.97730	3.26920	3.42799

of an internally pressurized cylinder for a plane stress load condition, showing marginal changes in the position of the radial homogeneous strips. Moreover, for this particular geometry and applied load condition, it is shown that both Voigt and Reuss estimates for Young's modulus and Poisson's ratio do bound estimates by means of the other micromechanical models.

5.3.3. Consideration of thermal loads

Finally, the consideration of thermal loads along the radial direction of the pressurized cylinder is addressed. The inclusion of such situation is recast by adding the term $\alpha(r)\Delta T(r)$ to both radial and hoop strains, where α is the secant coefficient of thermal expansion, $\Delta T(r) = T(r) - T^{ref}$ with T^{ref} is the reference temperature for zero thermal stress and T is the temperature along the cylinder thickness. Denoting by $\lambda(r)$ the thermal conductivity along the radius and letting y_3 and y_4 be the states corresponding to the temperature and the radial component of the heat flux, respectively, the material optimization problem associated with the thermomechanically loaded cylinder in the plane stress condition can be formulated as follows.

Problem 6. Find the distribution of the metallic volume fraction $V^*_m(r)$ along the radial direction of the cylinder so that the maximum Tresca stress is minimized, i.e.,

$$
\begin{aligned}
\min_{V_m(r)} \quad & \sigma^{T}_{eq,max} = \left\{ \int_{R_i}^{R_o} \left(E(r)\frac{y_1(r)}{r} + (\nu(r)-1)y_2(r) \right.\right. \\
& \left.\left. - \alpha(r)E(r)\left(y_3(r) - T^{ref}\right)\right)^{\mathcal{P}} dr \right\}^{1/\mathcal{P}} \\
\text{s.t.} \quad & y_1'(r) = -\frac{\nu(r)}{r}y_1(r) + \frac{1-\nu(r)^2}{E(r)}y_2(r) + \alpha(r)(1+\nu(r))y_3(r)\,, \\
& y_2'(r) = \frac{E(r)}{r^2}y_1(r) + \frac{\nu(r)-1}{r}y_2(r) - \frac{\alpha(r)E(r)}{r}\left(y_3(r) - T^{ref}\right)\,, \\
& y_3'(r) = \frac{y_4(r)}{r\lambda(r)}\,, \\
& y_4'(r) = 0\,, \\
& y_2(R_i) = -p_i\,, \\
& y_2(R_o) = 0\,, \\
& y_3(R_i) = T_i\,, \\
& y_3(R_o) = T_o\,, \\
& 0 \le V_m(r) \le 1\,,
\end{aligned}
\tag{79}
$$

where R_i, R_o, p_i, T_i, T_o, T^{ref} and $\mathcal{P}$ are given constants and $E(r)$, $\nu(r)$, $\alpha(r)$ and $\lambda(r)$ are linked to $V_m(r)$ through (1) or (2).

For the sake of illustrating an example, let $p_i = 10$ MPa, $T^{ref} = 0$ °C and $T_o = 20$ °C. Moreover, let the secant thermal expansion coefficient and the thermal conductivity obey both Voigt and Reuss rules of mixture, taking $\alpha_m = 1.2 \times 10^{-5}$ 1/°C, $\alpha_c = 0.8 \times 10^{-5}$ 1/°C, $\lambda_m = 0.040$ W/m°C and $\lambda_c = 0.018$ W/m°C. Figs. 13(a) and 13(b) show the best metallic volume fractions along the radial direction to achieve the lowest maximum value of the Tresca equivalent stress when the temperature at the inner boundary is 100 °C and 150 °C, respectively, and taking into account Voigt and Reuss rules of mixture. It is shown that there is a preference to adopt a more ceramic-based graded structure at the inner boundary, in contrast to solutions found before when the mechanical load was acting alone (see Figs. 7(a) and 7(b), where the temperature and stress distributions associated with the optimal volume fractions have been also shown, for both rules of mixture). As dictated by boundary conditions, the temperature distribution decreases from T_i to T_o along the radial direction. It is worth noting that, for fixed values of the applied loads, the adoption

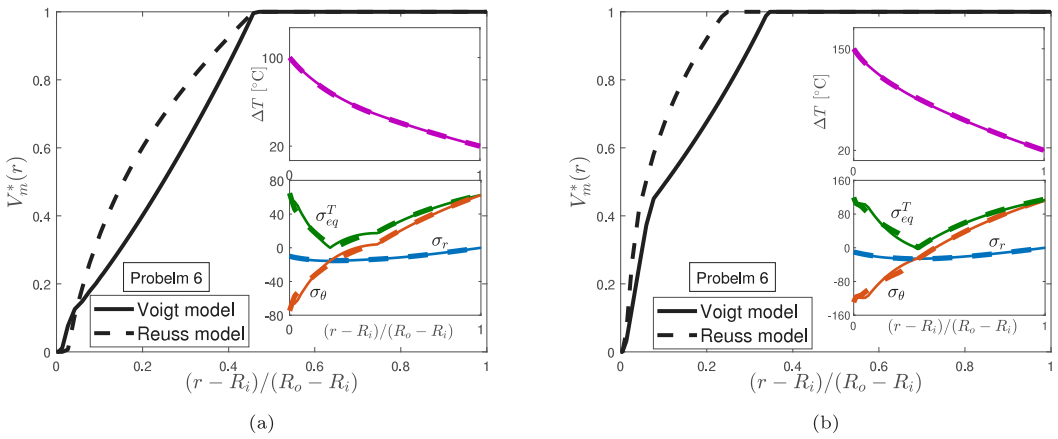

Fig. 13. Best metallic volume fractions, temperatures and stresses for the thermomechanically loaded cylinder of Problem 6 for (a) T_i = 100 °C and (b) T_i = 150 °C. Solid and dashed lines correspond to Voigt and Reuss models, respectively.

of one rule of mixture than another does not considerably affect the temperature and stress distributions, although might apparently alter the microstructure composition. This is in agreement with the former findings in Figs. 6(a) and 6(b) and Table 2 albeit the absence of thermal loads.

6. Conclusions

The optimization of the volume fraction distribution to minimize peak stresses in functionally graded cylinders, disks and spheres is addressed. The associated optimization problems have been stated and formulated as dynamic optimization problems by adopting two different classes of state variables. The advantage of this (tailoring) approach is that the variation of the decision variable, namely the volume fraction, is unknown beforehand and not limited to specified functions (e.g., the power-law function) but is searched among all possible functions (exhibiting a minimum degree of regularity such as piecewise continuity). Critical remarks on a previous effort to find optimal solutions analytically are reported, obliging one to resort to numerical methods.

Among all, we have shown that pseudospectral methods based on the state approximation by means of Lagrange interpolation polynomials and the governing equation collocation at a set of Gaussian quadrature points (Legendre–Gauss–Radau points) can be effectively applied. The application of such approach leads to the transcription of the dynamic optimization problems into nonlinear programming problems, whose solutions have been iteratively found by dedicated solvers. Expressions for the gradient of the objective functions as well as the Jacobian of the constraints have been derived through a sensitivity analysis, in order to reduce the functions evaluations at each iteration.

Most of the analyses have been carried out by considering the well-known Reuss and Voigt models. However, other models for the effective properties can be fitted in the same framework. As far as the loads are considered, the method can be applied to both mechanical and thermal loads. Optimal solutions for the volume fractions strongly depend on the geometry, the applied loads and their entity. In any case, optimal solutions yield enhanced stresses when compared to those associated with common volume distributions available in the literature, showing that the more general approach described in the paper leads to better engineering solutions. The application of the present numerical approach can be extended to numerous axisymmetric problems in the realm of mechanical engineering ranging from the search for thickness distributions for rotating disks complying with stress and mass constraints to the best arrangement of lay-up angles in multi-layered filament-wound composite pipes under thermomechanical loads. Eventually, further enhancement could be achieved by using nonsmoothness detection and mesh density reduction through an adaptive mesh refinement method.

CRediT authorship contribution statement

Hassan Mohamed Abdelalim Abdalla: Conceptualization, Methodology, Formal analysis, Software, Investigation, Validation, Writing – original draft. **Djaffar Boussaa:** Methodology, Formal analysis, Writing – review & editing. **Roberta Sburlati:** Formal analysis, Investigation, Validation, Writing – original draft. **Daniele Casagrande:** Validation, Writing – original draft.

Declaration of competing interest

The authors declare that they have no known competing financial interests or personal relationships that could have appeared to influence the work reported in this paper.

Data availability

Data will be made available on request.

References

[1] Miyamoto Y, Kaysser WA, Rabin BH, Kawasaki A, Ford RG. Functionally graded materials: Design, processing and applications. London: Kluwer Academic Publishers; 1999.
[2] Jafari S, Hojjati MH, Fathi A. Classical and modern optimization methods in minimum weight design of elastic rotating disk with variable thickness and density. Int J Press Vessels Pip 2012;92:41–7.
[3] Wang ZW, Zhang Q, Xia LZ, Wu JT, Liu PQ. Stress analysis and parameter optimization of an FGM pressure vessel subjected to thermo-mechanical loadings. Procedia Eng 2015;130:374–89.
[4] Khorsand M, Tang Y. Design functionally graded rotating disks under thermoelastic loads: Weight optimization. Int J Press Vessels Pip 2018;161:33–40.
[5] Abdalla HMA, Casagrande D, Moro L. Thermo-mechanical analysis and optimization of functionally graded rotating disks. J Strain Anal Eng Des 2020;55(5–6):159–71.
[6] Turteltaub S, Washabaugh P. Optimal distribution of material properties for an elastic continuum with structure-dependent body force. Int J Solids Struct 1999;36(30):4587–608.
[7] Turteltaub S. Optimal control and optimization of functionally graded materials for thermomechanical processes. Int J Solids Struct 2002;39(12):3175–97.
[8] Turteltaub S. Optimal non-homogeneous composites for dynamic loading. Struct Multidiscip Optim 2005;30:101–12.
[9] Boussaa D. Optimizing the composition profile of a functionally graded interlayer using a direct transcription method. Comput Mech 2006;39:59–71.
[10] Boussaa D. Optimization of temperature-dependent functionally graded material bodies. Comput Methods Appl Mech Engrg 2009;198:2827–38.
[11] Nie J, Zhong Z, Batra RC. Material tailoring for functionally graded hollow cylinders and spheres. Compos Sci Technol 2011;71:666–73.
[12] Batra RC. Material tailoring and universal relations for axisymmetric deformations of functionally graded rubberlike cylinders and spheres. Math Mech Solids 2011;16(7):729–38.
[13] Ashjari M, Khoshravan MR. Mass optimization of functionally graded plate for mechanical loading in the presence of deflection and stress constraints. Compos Struct 2020;110:118–32.

[14] Carraturo M, Rocca E, Bonetti E, Homberg D, Reali A, Auricchio F. Graded-material design based on phase-field and topology optimization. Comput Mech 2019;64:1589–600.
[15] Liew KM, He XQ, Meguid SA. Optimal shape control of functionally graded smart plates using genetic algorithms. Comput Mech 2004;33:245–53.
[16] Wang C, Koh JM, Yu T, Xie NG, Cheong KH. Material and shape optimization of bi-directional functionally graded plates by GIGA and an improved multi-objective particle swarm optimization algorithm. Comput Methods Appl Mech Eng 2020;366:113017.
[17] Wang C, Yu T, Shao G, Bui TQ. Multi-objective isogeometric integrated optimization for shape control of piezoelectric functionally graded plates. Comput Methods Appl Mech Engrg 2021;377:113698.
[18] Thang PT, Nguyen-Thoi T, Lee J. Shape and material optimization for buckling behavior of functionally graded toroidal shells. Thin-Walled Struct 2011;157:107129.
[19] Hu T, Wang Y, Zhang H, Li H, Ding X, Izui K, et al. Topology optimization of coated structures with layer-wise graded lattice infill for maximizing the fundamental eigenfrequency. Comput Struct 2022;271:106861.
[20] Abdalla HMA, Casagrande D, Bona FDe. A dynamic optimization setting for functionally graded thick-walled cylinders. Materials 2020;13:3988.
[21] Abdalla HMA, Casagrande D. An intrinsic material tailoring approach for functionally graded axisymmetric hollow bodies under plane elasticity. J Elast 2021;144:15–32.
[22] Marcu GG, Abdalla HMA, Casagrande D. Less is better: Coated spherical vessels over-perform their entirely graded counterparts. Compos Struct 2021;276:114529.
[23] Abdalla HMA, Casagrande D. Direct transcription approach to dynamic optimization problems in engineering. J Appl Comput Mech 2022;8(2):605–16.
[24] Bohm H. Ashort introduction to basic aspects of continuum micromechanics. Rep. 206, Institute of Lightweight Design and Structural Biomechanics (ILSB), Vienna University of Technology; 2022.
[25] Akbarzadeh AH, Abedini A, Chen ZT. Effect of micromechanical models on structural responses of functionally graded plates. Compos Struct 2015;119:598–609.
[26] Barber JR. Elasticity, solid mechanics and its applications. vol. 172, Dordrecht: Springer; 2010.
[27] Kurrer KE. The history of the theory of structures. From arch analysis to computational mechanics. Berlin: Ernst & Sohn; 2008.
[28] Vullo V, Vivio F. Rotors: Stress analysis and design. New York: Springer Science & Business Media; 2013.
[29] Nikbakht S, Kamarian S, Shakeri M. A review on optimization of composite structures part II: Functionally graded materials. Compos Struct 2019;214:83–102.
[30] Atashipour SA, Sburlati R, Atashipour SR. Elastic analysis of thick-walled pressurized spherical vessels coated with functionally graded materials. Meccanica 2014;49(12):2965–78.
[31] Atashipour SA, Sburlati R. Electro-elastic analysis of a coated spherical piezoceramic sensor. Compos Struct 2016;156.
[32] Madan R, Bhowmick S. Limit elastic analysis of functionally graded rotating disks under thermo-mechanical loading. Int J Appl Mech 2021;13(3):2150033.
[33] Cais M, Casagrande D, Abdalla HMA. Peterson charts for functionally graded rotating hollow disks with an eccentric hole. In: Abdel Wahab M, editor. Proceedings of the 4th international conference on numerical modelling in engineering. NME 2021, Lect Notes Mech Eng, 2021, p. 25–32.
[34] Bahaloo H, Nayeb-Hashemi H. Stress analysis and thermoelastic instability of an annular functionally graded rotating disk. J Therm Stresses 2022;45(1):1–11.
[35] Eldeeb AM, Shabana YM, Elsawaf A. Particle swarm optimization for the thermoelastic behaviors of functionally graded rotating nonuniform sandwich discs. Arab J Sci Eng 2022.
[36] Kirk DE. Optimal control theory: An introduction. New York: Dover Publications; 2004.
[37] Sagliano M, Theil S, Bergsma M, D'Onofrio V, Whittle L, Viavattene G. On the radau pseudospectral method: Theoretical and implementation advances. CEAS Space J 2017;9:313–31.
[38] Rao AV. A survey of numerical methods for optimal control. Adv Astronaut Sci 2010;135(1):497–528.
[39] Rao AV, Benson DA, Darby C, Patterson MA, Francolin C, Sanders I, et al. Algorithm 902: GPOPS, a MATLAB software for solving multiphase optimal control problems using the Gauss pseudospectral method. ACM Trans Math Software 2010;37(2):22:1–39.
[40] Garg D, Patterson MA, Darby C, Francolin C, Huntington GT, Hager WW, et al. Direct trajectory optimization and costate estimation of finite-horizon and infinite-horizon optimal control problems using a radau pseudospectral method. Comput Optim Appl 2011;49:335–58.
[41] Wang Y, Zhu Y, Jiang X, Li S. Comparison of LPM, GPM and RPM for optimization of low-thrust Earth-Mars rendezvous trajectories. In: Proceedings of 2014 IEEE Chinese guidance, navigation and control conference. Yantai, China; 2014.
[42] Abdalla HMA. Pseudospectral approach to the shape optimization of beams under buckling constraints. Eur J Comput Mech 2022;31(3):351–86.
[43] Patterson MA, Rao AV. Exploiting sparsity in direct collocation pseudospectral methods for solving optimal control problems. J Spacecr Rockets 2012;49(2):364–77.
[44] Hill R. Theory of mechanical properties of fibre-strengthened materials: I. Elastic behaviour. J Mech Phys Solids 1964;12(4):199–212.
[45] Zimmerman RW. Behavior of the Poisson ratio of a two-phase composite material in the high-concentration limit. Appl Mech Rev 1994;47(1S):S38–44.
[46] Zuiker JR. Functionally graded materials: Choice of micromechanics model and limitations in property variation. Compos Eng 1995;5(7):7807–19.
[47] Sburlati R, Cianci R. Shear modulus prediction of a particulate composite reinforced with hollow spheres surrounded by a graded interphase. Compos Struct 2020;250:112528.
[48] Madan R, Bhowmick S. Modeling of functionally graded materials to estimate effective thermo-mechanical properties. World J Eng 2021;19(3):291–301.